Plasmonic phenomena in molecular junctions: principles and applications

Maoning Wang[1,2], *Tao Wang*[3,4], *Oluwafemi S. Ojambati*[5], *Thorin Jake Duffin*[4,6], *Keehoon Kang*[7], *Takhee Lee*[8]✉, *Elke Scheer*[2]✉, *Dong Xiang*[1]✉ *and Christian A. Nijhuis*[4,6,9]✉

Abstract | Molecular junctions are building blocks for constructing future nanoelectronic devices that enable the investigation of a broad range of electronic transport properties within nanoscale regions. Crossing both the nanoscopic and mesoscopic length scales, plasmonics lies at the intersection of the macroscopic photonics and nanoelectronics, owing to their capability of confining light to dimensions far below the diffraction limit. Research activities on plasmonic phenomena in molecular electronics started around 2010, and feedback between plasmons and molecular junctions has increased over the past years. These efforts can provide new insights into the near-field interaction and the corresponding tunability in properties, as well as resultant plasmon-based molecular devices. This Review presents the latest advancements of plasmonic resonances in molecular junctions and details the progress in plasmon excitation and plasmon coupling. We also highlight emerging experimental approaches to unravel the mechanisms behind the various types of light–matter interactions at molecular length scales, where quantum effects come into play. Finally, we discuss the potential of these plasmonic–electronic hybrid systems across various future applications, including sensing, photocatalysis, molecular trapping and active control of molecular switches.

Molecular junctions
Molecular monolayers or single molecules sandwiched between two (metal) electrodes.

Mechanically controllable break junctions
(MCBJs). Adjustable nanogap widths with sub-angstrom precision can be obtained in MCBJs by mechanically controlled bending of the substrate, which effectively stretches the suspended nanowire on top of the substrate until the nanowire breaks.

✉*e-mail:* *tlee@snu.ac.kr; elke.scheer@uni-konstanz.de; xiangdongde@nankai.edu.cn; c.a.nijhuis@utwente.nl*

https://doi.org/10.1038/s41570-022-00423-4

Molecular electronics is an attractive research field for upcoming technologies, including soft robotics[1], brain-inspired computing[2–4] and biocompatible electronics[5–7]. It has the potential to reduce power consumption and device footprint area to molecular length scales owing to its highly complementary nature with contemporary metal oxide-based technologies[8]. Since the pioneering proposal of a single-molecule rectifier by Ratner and Aviram in 1974 (REF.[9]), versatile functionalities of molecular junctions have been demonstrated, including molecular rectifiers, transistors, switches, memory and sensors[10–14]. This increased focus on studying charge transport processes at the molecular length scale has been enabled by the development of reliable experimental tools, including scanning tunnelling microscope break junctions (STM-BJs)[15,16], mechanically controllable break junctions (MCBJs)[17,18], electromigration break junctions (EBJs)[19–21], junctions formed with atomic force microscope (AFM) tips as the top electrodes (AFMJs)[22], nanoparticle on mirror molecular junctions (NPoMJs)[23,24], high-quality self-assembled monolayer (SAM)-based tunnelling junctions (STJs)[25,26] and electrochemical deposition-based molecular junctions[27–29]. Combined with the novel, fast-developing fabrication techniques for nanoscale patterning and structuring of materials, there has been a significant increase in the innovation of nano-optics — especially plasmonics — over the past two decades[30,31]. As summarized in this Review, plasmonic resonances, especially those in molecular junctions, offer unique pliability in both tuning the electromagnetic environment of a molecular junction and modifying the charge transport characteristics in the quantum mechanical tunnelling regime. These capabilities can enable exceptional control over the optoelectronic properties at the molecular length scales[32] with potential applications in metasurfaces[33], nanoscale light sources[34], solar energy conversion[35] and quantum optomechanics[36].

Surface plasmons can exist as either propagating modes along a surface or confined nanoparticle resonances, termed surface plasmon polaritons (SPPs) and localized surface plasmons (LSPs), respectively (FIG. 1a). Highly tunable surface plasmon modes generated in nanostructures and nanogaps enable highly confined fields that can modify the local electromagnetic environment, where charge carriers transport across molecular junctions[37] (FIG. 1a).

Generally, the tunability of the plasmonic interaction with tunnelling electrons in molecular junctions depends on a few factors. First, the geometry of the nanostructure (FIG. 1a). The nanoscale resonant electrodes can behave as antennas upon external irradiation (FIG. 1b–f),

Electromigration break junctions
(EBJs). Stable nanogaps as small as 1–3 nm in EBJs are made by increasing the current density in a thin metal wire, leading to precisely controlled electromigration of metal atoms and eventual breakage of the wire.

Surface plasmons
Coherent, collective oscillations of free electrons at dielectric–metal interfaces.

Floquet states
Eigenstates of electrons in time-periodic fields, equivalent to Bloch states in spatially periodic fields.

whereas non-resonant larger-area, plane–plane junctions allow SPPs to propagate into an external waveguide[38–40] (FIG. 1g). Second, the relative permittivity of the embedding medium may have a significant influence on the plasmonic response of the system[41–44]. Finally, the excitation approaches of the plasmonic system which include the electrical excitation of cavity plasmons and the optical excitation of resonant plasmonic cavity modes, which can excite both radiative and non-radiative electromagnetic modes. This tunability has been exploited in different architectures to elicit efficient interplay between the resonant response of the plasmonic nanostructures and charge transport across molecular junctions[45–48] where quantum effects cannot be ignored[37], thus bridging the research fields of nano-optics and molecular electronics. The integrating aspects of physics, chemistry, materials science and engineering in plasmonic molecular junctions enable novel optoelectronic properties and devices[49].

Several reviews summarize different molecular junctions under optical excitation (see REFS.[23,24,37,47,50–53]), addressing fundamental and applied aspects. In this Review, we summarize the phenomena and mechanisms of plasmonic interactions with molecular junctions, and try to clarify how different languages and models have been established in the individual disciplines. The various architectures within the three broad groups — namely, point–point junctions, point–plane junctions and plane–plane junctions (FIG. 1a) — are then introduced. Subsequently, recent experimental advances and different characterization techniques in molecular-plasmonic systems under voltage bias and optical excitation approaches are highlighted. Plasmon–molecule coupling and how this modifies the electromagnetic environment and the charge transport characteristics across the molecular layer is also explored. Finally, the emerging applications in plasmon–molecule hybrid structures are described followed by an overview of what to expect in the future.

Mechanisms of plasmonic interactions

The various mechanisms and phenomena related to the interplay of plasmon excitations, junction geometry and charge transport mechanisms in molecular junctions are presented in this section (FIG. 2). Owing to the interdisciplinary character of the field, different names are used for the same phenomenon across subdisciplines. On the other hand, different meanings can be assigned to the same term. For example, the term 'hot electron' is used with different meanings, often resulting in ambiguities[54,55]. Therefore, we present the most important phenomena that are associated with plasmonics and molecular transport in this section and unify terminologies across multiple fields. We note that in this Review the optical fields are assumed to be small enough not to dress the states of the molecules, which would result in Floquet states and multi-photon absorption, as this would require V_{opt} in the order of the molecular level spacing. In general, plasmonic gaps can only withstand a limited field strength before melting and reshaping, which also limits the occurrence of dressed states[56].

Optoelectronic effects in junctions

Photo-assisted tunnelling. The term photo-assisted tunnelling (PAT) (FIG. 2a) denotes a change of the charge transport across a junction upon light absorption in the metallic electrodes. Strictly speaking, PAT refers to absorption in the metallic electrodes, but in the context of molecular junctions it has been widened to also include absorption in the molecule, which is usually negligible. Therefore, PAT is not specific to molecular junctions but exists also in junctions with, for instance, metal oxide nanogaps. PAT works, in principle, for arbitrarily small photon energies ($\hbar\omega$), and hence does not require changes in the charge state of the molecule by exciting an electron from the HOMO to the LUMO, as is occasionally anticipated. The latter would correspond to hot-electron photochemistry, as described below. For the case of coherent charge transport, the current I as a function of the voltage V across the molecular junction can be estimated by the Landauer formalism[57]:

$$I[V,T(E)] = \frac{G_0}{e}\int_{-\infty}^{\infty} T(E)\left[f_L\left(E+\frac{eV}{2}\right)-f_R\left(E-\frac{eV}{2}\right)\right]\mathrm{d}E \quad (1)$$

where $I[V,T(E)]$ is the current, e is the elementary charge, G_0 is the conductance quantum, equal to $2e^2/h$ (where h is Planck's constant), V is the applied bias voltage, f_L and f_R are the equilibrium Fermi distributions of the left and right electrodes, respectively, and $T(E)$ is the electronic transmission function. The energy E is measured with respect to the Fermi energy of the electrodes. The PAT process is described as a change of the transmission function $T(E)$ to a new transmission function $T'(E)$[58,59]:

$$T'(E) = \sum_{n=-\infty}^{\infty} J_n^2\left(\frac{eV_{opt}}{\hbar\omega}\right)T(E+n\hbar\omega) \quad (2)$$

where V_{opt} is the amplitude of the alternating voltage generated across the junction by the light, J_n denotes the nth-order Bessel function of the first kind, $\hbar\omega$ is the photon energy and e is the electron charge. The square of the Bessel function gives the probability of absorbing or emitting n photons. Equation (2) shows that the energy relevant for the transmission of the electrons is shifted

Author addresses

[1]Institute of Modern Optics and Center of Single-Molecule Sciences, Nankai University, Tianjin Key Laboratory of Micro-Scale Optical Information Science and Technology, Tianjin, China.
[2]Department of Physics, University of Konstanz, Konstanz, Germany.
[3]Jiangsu Key Laboratory for Carbon-Based Functional Materials & Devices, Soochow University, Suzhou, Jiangsu, China.
[4]Department of Chemistry, National University of Singapore, Singapore, Singapore.
[5]Dynamic Nanophotonics, MESA+ Institute for Nanotechnology, Faculty of Science and Technology, University of Twente, Enschede, The Netherlands.
[6]National University of Singapore Graduate School for Integrative Sciences and Engineering, National University of Singapore, Singapore, Singapore.
[7]Department of Materials Science and Engineering, Research Institute of Advanced Materials, and Institute of Applied Physics, Seoul National University, Seoul, Korea.
[8]Department of Physics and Astronomy, and Institute of Applied Physics, Seoul National University, Seoul, Korea.
[9]Department of Molecules and Materials, MESA+ Institute for Nanotechnology and Center for Brain-Inspired Nano Systems, Faculty of Science and Technology, University of Twente, Enschede, The Netherlands.

by integer multiples of $\hbar\omega$. The process can be seen as an alternating voltage across the junction that makes the Fermi energy oscillate by this voltage. In the case of molecular junctions, $T(E)$ varies on a small energy scale, such that PAT may enhance the transmission probability by several orders of magnitude.

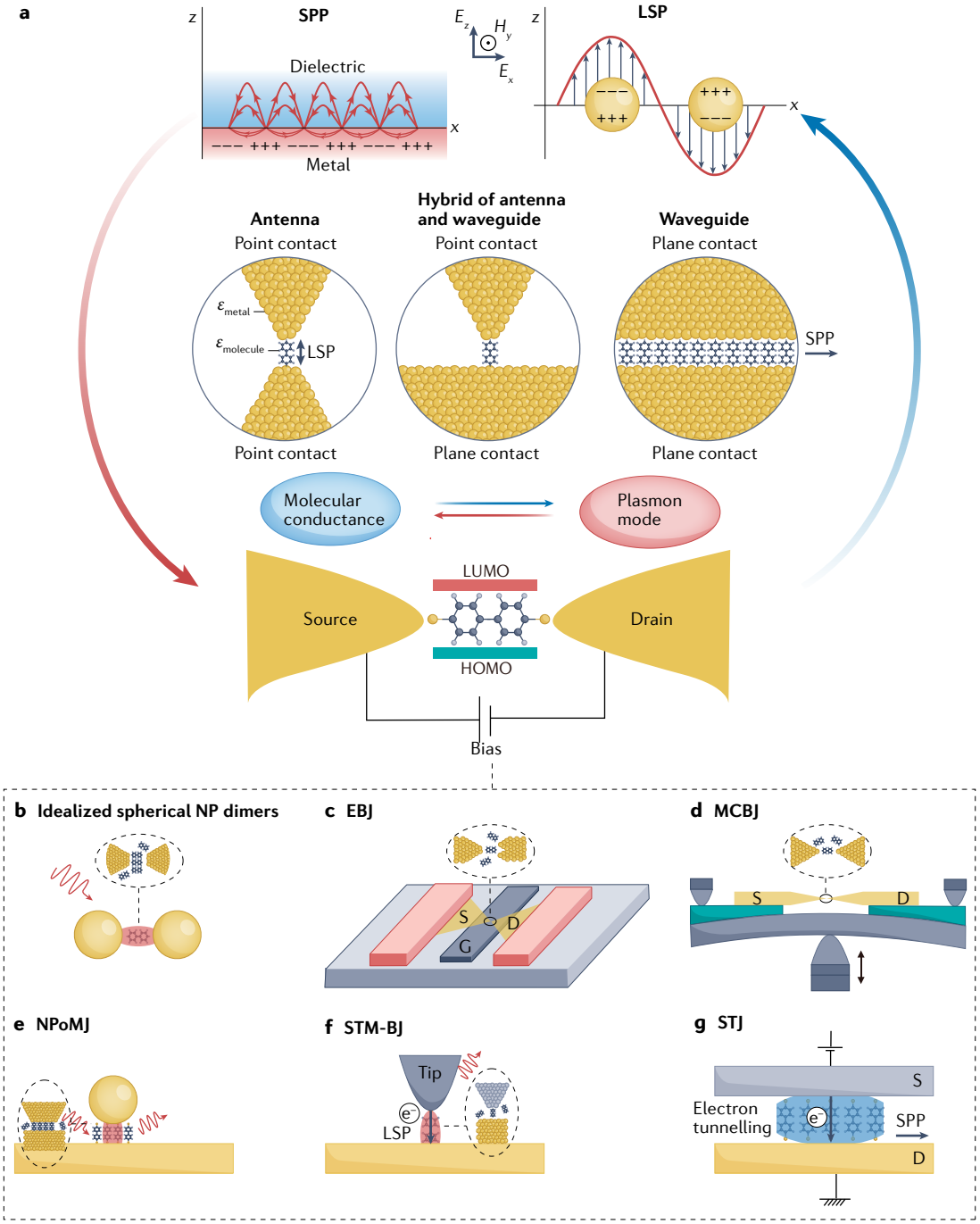

Fig. 1 | **Interplay between plasmonics and molecular junctions. a** | Surface plasmon polariton (SPP) (top left) and localized surface plasmon (LSP) (top right) with the field lines and orientation shown, along with different plasmonic junction geometries (point–point junctions, point–plane junctions and plane–plane junctions) and the permittivity (ε) of the material media. Here, we define a 'point' as a nanostructure that supports LSPs whereas a plane supports SPPs. A 'point–point junction' is coupled plasmonic antennas whereas a 'plane–plane junction' serves as a waveguide. The 'point–plane junction' is a hybrid of an antenna and the waveguide. **b**–**g** | Different plasmonic molecular electronic systems: nanoparticle dimer (NP dimer) (panel **b**), electromigration break junction (EBJ) (panel **c**), mechanically controllable break junction (MCBJ) (panel **d**), nanoparticle on mirror molecular junction (NPoMJ) (panel **e**), scanning tunnelling microscope break junction (STM-BJ) (panel **f**) and self-assembled monolayer (SAM)-based tunnelling junction (STJ) (panel **g**). These nanostructures typically have electrodes act as a source (S) and a drain (D), and some have an additional gate (G) electrode to control electronic transport. Panels **b**–**f** show idealized structures and surfaces, but the surfaces are complex containing nanoscale corrugation and grains in reality as highlighted in the blow-ups.

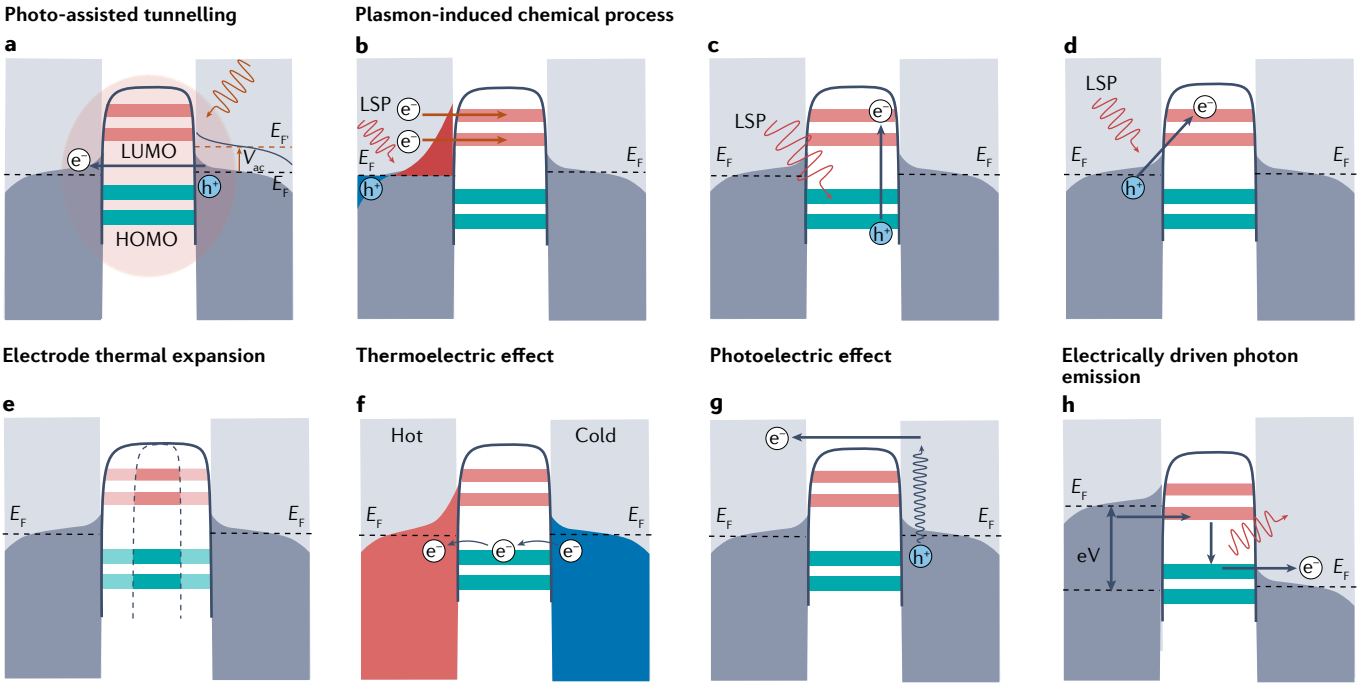

Fig. 2 | **Different types of plasmon-induced charge transport processes across metal–molecule structures. a** | Photo-assisted tunnelling (PAT) changes the transmission of a molecular junction by acquiring energy from the optical field. Incident light illuminates the whole junction. V_{ac} is the voltage drop across the junction caused by the incident electromagnetic field. **b**–**d** | Plasmon-induced chemical processes with different paths: indirect hot-electron transfer generated by localized surface plasmon (LSP) decay heats up the Fermi sea of one electrode, followed by injection into the LUMO to form a transient negative ion state of the molecule (panel **b**); direct intramolecular excitation mechanism — a resonant LSP directly induces excitation from the HOMO to the LUMO in the molecule (panel **c**); and charge transfer from the surface states of the metal electrodes to the LUMO (panel **d**). **e** | The effective tunnel barrier between the source and drain electrodes is altered due to thermal expansion of the plasmon-induced heating of the phonon bath of the electrodes, resulting in a reduced gap size. **f** | Thermoelectric transport across the junction in an open-circuit set-up under an applied temperature difference ($T_{hot}-T_{cold}$). Red and blue regions represent hot and cold parts. **g** | Direct absorption of a photon by the metal electrode emits a photoelectron with sufficient energy and appropriate momentum to exceed the effective barrier for tunnelling. **h** | If a sufficient bias is applied to the junction, the molecule can modulate the photon emission through inelastic tunnelling between the HOMO and the LUMO, thereby transferring electrons. Left and right dashed lines represent the Fermi levels (E_F) of the metal electrodes, and grey represents the occupation of electronic states in the metal electrodes. Coloured stripes in the middle illustrate the HOMO and LUMO of the molecule.

Optical rectification. When an optical field (with an amplitude V_{opt} and energy $\hbar\omega$) that illuminates a nanojunction is small, such that $eV_{opt} \ll \hbar\omega$, multiple-photon absorption and emission processes ($|n|>1$, where n is the number of photons) can be neglected. According to the Tien and Gordon formula[60,61], the existence of an incident plasmonic field can be equivalent to an effective alternating current bias $V_{ac}\cos(\omega t)$, which adds to the original direct current tunnelling current, leading to optical rectification[62–64]. Here, ω is the frequency of the plasmon, V_{ac} is the amplitude of the alternating current bias and t represents time. Under the condition $eV_{opt} \ll \hbar\omega$, with the tunnelling non-linearity small on the voltage scale $\hbar\omega/e$, the increased current ΔI_{dc} can be simplified to:

$$\Delta I_{dc} = \frac{1}{4} V_{ac}^2 \cdot \left.\frac{d^2 I}{dV^2}\right|_{V=V_{dc}} \quad (3)$$

by retaining the lowest order terms $n = 0, \pm 1$ in the asymptotic forms of J_n as shown in Eq. (2). Optical rectification occurs in small junctions when the electrons are able to follow the rapid oscillations of the illuminating optical field, and thereby harness the second-order non-linearities of the tunnelling probability[65] (see Eq. (3)). Optical rectification in molecular junctions has to be distinguished from molecular rectification of currents (molecular equivalent of a diode). This latter effect denotes asymmetric I–V values of molecular junctions resulting from asymmetric electrode coupling or in-built asymmetries in the molecule, and this process occurs without illumination.

Plasmon-induced hot-electron generation

A widely used concept in the context of plasmonic junctions are hot electrons (or, more generally speaking, hot charge carriers). In most cases it is unclear how to distinguish experimentally between hot-electron phenomena and PAT[58,64], and the term 'hot electrons' is used in different meanings. Below we describe different phenomena ascribed to hot electrons.

Hot-electron generation. When light at frequencies close to the plasma frequency illuminates a metallic nanostructure, plasmons decay through either radiative photon re-emission or non-radiative generation of highly energetic charge carriers (denoted as hot carriers) via Landau damping on a timescale ranging from 1 to 100 fs[66]. The energies of these hot carriers are much larger than those in the background thermal distribution, thereby enabling processes that are not possible

with thermalized carriers. Hence, this system is out of equilibrium where hot carriers can transfer energy and shift to nearby molecules and induce catalytic[67,68] and electrochemical reactions[69,70].

Hot-electron transport. If the hot-electron generation occurs very close to the junction (within the inelastic scattering length for excitations with such high energy), individual hot electrons may be transported across the junctions immediately after their excitation (within a few femtoseconds after their creation) and will contribute to the charge current[71]. The hot electrons may scatter with each other and give rise to heating of the whole electron gas, thus forming a broader Fermi edge, but the lattice will still be cold. Therefore, the electron temperature can be much higher than the lattice temperature[72,73]. During this process, hot carriers may cause additional contributions to the current through molecular junctions if they tunnel across the junction[74]. An imbalance in hot-electron production between the two electrodes may lead to a net current to be measured at zero bias. The imbalance can be caused by using electrodes with different materials, different local nanoscale geometries or different coupling Γ with the molecule, resulting in different plasmon absorption and hot-electron transfer rates at both sides of the junction. Here, Γ is the energy-independent broadening of the molecular resonance coupled to the electrodes and is inversely proportional to the charge transfer time. The hot electron-induced current magnitude is also dependent on the polarization, wavelength and plasmon intensity[58]. Discriminating between PAT and hot electrons is only possible in transient situations, as in steady state they are identical[58,64]. Thus, one option includes using junction systems with small coupling Γ to increase the charge transfer time with respect to the lifetime of hot electrons with time-resolved measurements[58,75]. In support of further studies in the terahertz regime, employing illumination frequencies far below the plasma frequency is effective at reducing the energy absorption by the electrodes and minimizes the creation of hot-electron distributions[76,77].

Equilibration of electrons. The transported hot electrons eventually equilibrate with the Fermi sea and the lattice on the timescale of the (inelastic) electron–phonon scattering time. The absolute timescale crucially depends on the electronic diffusion constant of the electrodes and the temperature of the system. For metal electrodes at room temperature, this timescale is in the order of picoseconds but may increase to a few nanoseconds at very low temperatures[73,78]. The equilibration process creates heat (phonons), resulting in a higher lattice temperature. This increase in the temperature leads to thermal expansion (detailed below) and an increase in reaction rates[79]. The latter complicates the discrimination between increasing chemical reaction rates by hot electrons or simply by heating[54,67,80,81].

Hot-electron photochemistry. Highly energetic hot-carrier pairs are generated in the metal electrodes by non-radiative decay of the LSP (FIG. 2b), and these hot electrons indirectly transfer to the molecule to form a transient negative ion[82]. A direct intramolecular excitation mechanism is proposed in FIG. 2c in which the LSP resonantly excites electrons from the HOMO to the LUMO of a molecule[83]. In addition, charge transfer from the valence band of the metal electrode near E_F to the LUMO of the molecule also contributes to plasmon-induced chemical transformation[84] (FIG. 2d), where the process is referred to as chemical interface damping[85–88]. The equivalent mechanism exists for hot holes that, accordingly, form a transient positive ion and transfer to the HOMO[89]. Hot-electron photochemistry at organic semiconductor interfaces is distinctive from the role of both highly energetic carriers and hot-electron transport added to the current across molecular junctions. In addition to requiring carriers far from the Fermi level to more efficiently drive reactions in molecules, the collection of hot carriers at the surface of the plasmonic nanostructure with minimal scattering is also required to achieve high quantum efficiencies[90]. Finally, photon energy, polarization, molecular arrangement, interfacial electronic coupling, molecular energy-level distribution and the metal nanostructure configuration have to be considered to minimize the energy loss during this transport and collection[91,92].

Accompanying effects in junctions

In general, several unwanted side effects may occur beyond the mainly envisaged direct electronic phenomena caused by irradiating plasmonic junctions. These have to be accounted for in real experiments as they may obscure the direct effects. Moreover, the underlying functional principles of the side effects may lend themselves to build functional devices.

Electrode thermal expansion. The increased lattice temperature by LSP decay into phonons in the electrodes may reduce the junction gap to some extent so that the effective tunnel barrier between the electrodes is shortened (FIG. 2e). Thermal expansion of bare metallic electrodes under direct illumination has been verified in various realizations of junctions resulting in reversible plasmon heating-induced atomic switches[93–96]. In some of the experiments, the junctions were indirectly illuminated — the light irradiates the left/right side of the electrode rather than the junction itself — to reduce the thermal expansion effect. However, it is a great challenge to realize strain-free electrodes, and contributions due to thermal expansion to the observed plasmon-induced conductance changes thus cannot be neglected[97–99].

Thermoelectric effect. Induced temperature gradients across the junction (FIG. 2f) are either due to a spatially inhomogeneous distribution of the illuminating laser beam cross-section or due to geometric differences between the two electrodes that may give rise to a thermoelectric current[100,101]. The thermoelectric current I_{th} without external bias can be written as:

$$I_{th} = GS\Delta\Theta \tag{4}$$

where the Seebeck coefficient S determines the magnitude of the built-in potential across the junction

Excitons
Excitons can form when a molecule emitter absorbs photons where the frequency is in or close to resonance with the HOMO–LUMO gap. This process excites an electron from the HOMO into the LUMO, consequently resulting in the Coulomb attraction between the electron in the LUMO and the positive hole left behind. An exciton is such a bound state. When an exciton recombines radiatively, a photon is emitted.

when a temperature difference $\Delta\Theta$ is applied and G is the electrical conductance. The Seebeck coefficient is given by:

$$S(E_F) = \frac{\pi^2 k_B^2 \Theta}{3eT(E)} \frac{dT(E)}{dE}\bigg|_{E=E_F} \quad (5)$$

where $T(E)$ is the transmission function, Θ is the average temperature of left and right leads, E_F is the Fermi energy of the leads and k_B is the Boltzmann constant. The temperature difference $\Delta\Theta$ causes an unequal electronic distribution in the electrodes. As Eq. (5) shows, this results in a net current at zero voltage if $T(E)$ has a final slope at the Fermi energy.

External photon emission. Photoelectrons can be generated (FIG. 2g) without an external bias, which depends on the energy of the incident photons and the effective work function of the metal electrodes. The process requires sufficient energy for an electron to exceed the effective barrier for tunnelling[102,103].

Electrical-driven photon emission. When an external bias voltage is applied across the junctions, plasmons can be excited by inelastic tunnelling. An inelastic tunnelling electron donates a fraction of its energy to create a plasmon, which is converted into photon emission by radiative decay of the plasmon[47] (FIG. 2h). Light emission from metal–insulator–metal (MIM) junctions depends on the applied bias voltage V_{appl}, and the cut-off frequency of the light emission follows the quantum relation: $h\nu_{cut\text{-}off} = eV_{appl}$ (REF.[104]).

Plasmon–exciton coupling in junctions

In the dark, the molecular junction conductance is dominated by tunnelling of electrons (holes) into the LUMO (HOMO) and the energy difference between the LUMO (HOMO) and the Fermi level of the metal. Under illumination, when the LUMO (HOMO) becomes partially filled, a charge entering the HOMO (LUMO) is Coulomb attracted to form bound electron–hole pairs (so-called excitons), resulting in an effective shift of the HOMO and LUMO levels[105]. The metal electrodes also provide screening to the HOMO, LUMO and the exciton states, such that a HOMO–LUMO gap renormalization occurs due to the Coulomb interaction between excitons and image charges in the metal electrodes[106]. When there is an exchange of photon energy between the cavity plasmons and the excitons, the two systems are said to be 'coupled', which is analogous to two coupled harmonic oscillators[107]. The coupling of plasmonic modes with molecular exciton states embedded in nanocavity junctions results in changes of the absorption spectra[108], scattering[109] and surface-enhanced fluorescence[110]. The spectrum indicates how a plasmonic nanocavity couples with emitters, such as dyes and fluorescent molecules, and classifies the transition from weak to strong coupling[111,112].

Definition of coupling parameters. The coupling strength g is the energy transfer rate between excitons and the nanocavity, and its value determines the regime of the coupling[113]. The cavity loss rate (γ_C) is the rate at which the radiative plasmonic modes emit to the environment. Outside the cavity, the excitons emit at a rate called the spontaneous emission decay rate γ (REF.[114,115]) (FIG. 3a).

Let us consider an emitter, characterized as a two-level system with a transition dipole moment μ from a ground state to an excited state and a resonance frequency ω_0. The plasmonic cavity has resonance frequency ω_c, cavity loss rate γ_C (also the inverse of the LSP lifetime determining the width of the resonance) and corresponding quality factor $Q = \omega_c/\gamma_c$. The value of Q quantifies the losses in the plasmon cavity and how

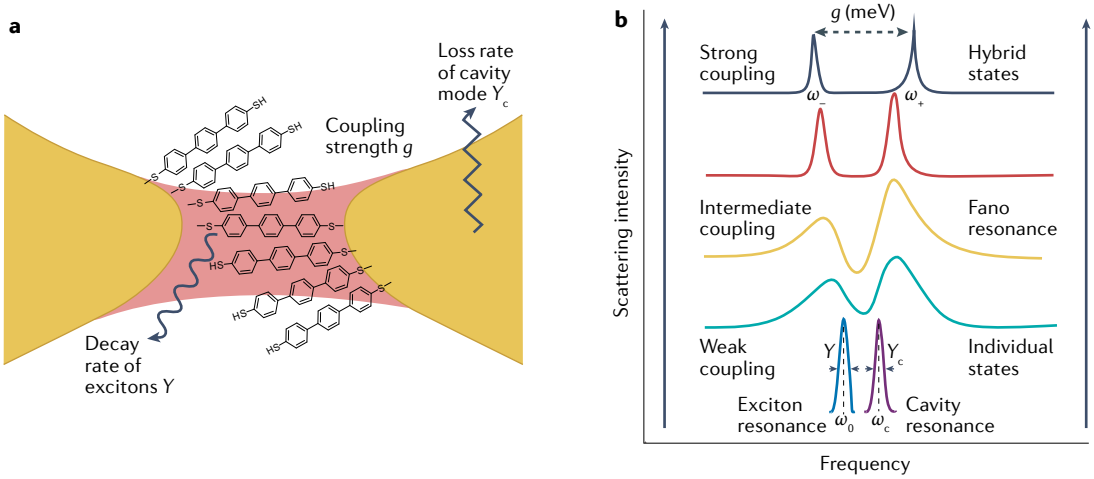

Fig. 3 | **Different coupling regimes in plasmon–exciton junctions. a** | Characteristic parameter diagram of plasmon coupling with excitons inside a cavity. γ is the decay rate of excitons, γ_C is the loss rate of the cavity mode radiated to the environment and g is the coupling coefficient of excitons and cavity plasmons. **b** | Transition of the spectral line shape from individual states to Fano resonance and, finally, to Rabi splitting as the plasmon–exciton coupling increases. ω_0 is the exciton resonance frequency, ω_p is the plasmon resonance frequency, and ω_+ and ω_- denote the split resonance frequencies of the plasmon–exciton hybrid states.

Fano interference
Generally speaking, Fano resonances occur when a discrete state and a continuous quantum mechanical state interfere. As a result, the line shape of their coupled resonance is altered: depending on the relative amplitude and phase of the two interfering states, the line shape may split up or change its shape to an anti-resonance. In the special case here, the two interfering states are the emission of the molecule in the junction and the continuum-like state of the plasmonic nanocavity.

Rabi splitting
When the coupling strength exceeds the dissipation rates of the coupled system of the emitter and cavity plasmons, new hybrid polariton modes can form. The new hybrid modes can appear as two distinct peaks in either scattering or emission spectra and the separation between the two peaks is proportional to the coupling strength *g*. This characteristic feature is called Rabi splitting.

efficiently it stores the plasmon energy. Equation (6) defines the coupling efficiency *g*:

$$g = \mu \sqrt{\frac{\hbar \omega_c}{2\varepsilon_0 \varepsilon_r V_{eff}}} \quad (6)$$

where ε_0 is the permittivity of the vacuum, ε_r is the relative permittivity and V_{eff} is the effective cavity mode volume[116]. The coupling efficiency *g* can be controlled by changing the cavity size, the cavity morphology, the relative permittivity inside the cavity or the orientation and location of the emitter inside the nanocavity[117,118]. The shape of the optical spectrum of the plasmon–exciton depends on the coupling strength, polarization, intensity enhancement or reduction, modulation of radiative and non-radiative decay rates, and more[119–123].

Classification of coupling regimes. A weak-coupling regime, defined by a coupling strength $g \ll \frac{1}{2}|\gamma - \gamma_C|$, occurs when the excitons and plasmons can be considered separate systems, and their interaction is described perturbatively between their uncoupled states. The energy of the modes does not change, and only the losses (decay) are modified[124,125] (FIG. 3). An intermediate-coupling regime with $\frac{1}{2}|\gamma - \gamma_C| < g < \sqrt{\frac{1}{2}(\gamma^2 + \gamma_C^2)}$ is where the exciton and plasmon modes start to have an energy-level interaction, which leads to a trough in the absorption/scattering spectrum owing to Fano interference[126]. The intermediate-coupling regime can be interpreted in the time domain as coherent energy transfer between the two modes being hindered by their large decay rates. The strong-coupling regime, where $g > \sqrt{\frac{1}{2}(\gamma^2 + \gamma_C^2)}$, in which new exciton–plasmon hybridized states are formed and energy is coherently exchanged, shows coupling strength-dependent Rabi splitting in the frequency domain[125–127].

Purcell effect (weak-coupling regime). The Purcell effect describes the modification of the spontaneous emission rate via a change in the photonic local density of states that quantifies the number of allowed modes per unit volume per frequency at the location of the emitter[128]. An increase in the local density of states thus implies that the cavity provides new decay channels for the emitter. The extent of the modification of the emission rate is given by the Purcell factor *P:*

$$P = \frac{3}{4}\frac{Q}{\pi}\frac{\lambda^3}{V_{eff}} \quad (7)$$

where $\lambda = 2\pi c/n\omega_c$ (c is the speed of light in a vacuum) is the photon wavelength and n is the index of refraction occupying the cavity[129]. Under the condition of $P \gg 1$, the cavity greatly reduces the emission lifetime, which means that the molecules emit faster[130]. The faster emission implies a higher radiative decay rate, which results in a higher quantum efficiency. The higher quantum efficiency makes weak emitters with low intrinsic quantum yield emit more brightly and the emission intensity of good emitters remains relatively unaltered[131]. The Purcell factor can be as high as 10^5–10^6 in plasmonic nanocavities, one of the most efficient systems for light–matter interactions[23].

The transition from weak to strong coupling. We give a brief description regarding the transition from weak to strong coupling here; for a more complete discussion on this topic, see REFS.[132–134]. The optical extinction and emission spectra line shapes depend on the coupling between the plasmonic and the molecular subsystems. The excitation rate of an emitter in the nanocavity is largely dependent on the overlap between the absorption of the emitter and the plasmonic nanocavity modes. On the other hand, the emission rate depends on the overlap of the emission spectrum with the nanocavity mode. As the system transitions from weak to strong coupling, the line shape changes from two individual distinct modes of the exciton and nanocavity resonances to two polaritonic modes (FIG. 3b). In the weak-coupling regime, the high local density of states in the nanocavity results in efficient excitation of emitting molecules. Thus, they rapidly relax from a higher energy level to lower energy levels, enabling surface-enhanced spectroscopy. The intermediate coupling requires the coupling strength *g* to be comparable with the emitter line width γ. This results in Fano interference between continuous plasmon resonances and discrete emitter energy levels, which appears as asymmetric peaks in the scattering spectrum. To realize the strong-coupling regime, *g* has to be increased or γ_C or γ has to be decreased such that $2g > \gamma, \gamma_C$ for sufficient energy exchange between the nanocavity and the exciton. For instance, γ can be decreased by increasing *Q*, which is generally a challenge in a plasmonic nanocavity, and *g* can be increased by increasing the molecular dipole moment μ and the electric field in the cavity or decreasing V_{eff}.

Plasmonic junction systems

The use of nanostructures, such as nanoantennas, nanoparticles, nanorods and nanotips, to form junctions can accommodate individual molecules[14] or an assembly of them[8,12,13,26,135]. These junctions can also serve as basic components to excite surface plasmons, enabling structural control to manipulate electromagnetic field strength[136], spatial energy distribution[137] and heat dissipation[138]. In this Review, we classify molecular junctions according to their architecture into point–point junctions, point–plane junctions and plane–plane junctions (FIG. 1a). Here, we define a 'point' and a 'plane' in a broad sense to include nanostructures that support localized and propagating surface plasmons, respectively, and hence the electrodes act as waveguides or as antennas. A point acts as a plasmonic antenna that radiates optical waves from near field to far field. The point–point contact nanostructures that we discuss below are thus two plasmonic antennas that are coupled together. At very small nanogaps, the coupled plasmons between the two points interact in the near field and form a nanocavity. Plane–plane contact nanostructures are effectively a waveguide (similar to an optical fibre), which confines in-plane electromagnetic modes in a dielectric insulating layer. The plane–plane contact nanostructures can be seen as MIM waveguides, also known as patch antennas[23], where the insulating dielectric medium is a molecular layer. The point–plane contact is a hybrid of a plasmonic antenna and a waveguide. As we discuss

Electron energy-loss spectroscopy
(EELS). An analysis tool to measure and map the energy of the inelastically scattered electrons in the low-loss region of 0.5–3.5 eV.

in this Review, the plasmonic modes of the point–plane contact have contributions from both antenna and MIM waveguide modes.

Therefore, the dimension of a 'point' ranges from a nanotip that can be a few atoms wide up to the facet of a nanoparticle (<50 nm) and a nanorod (~100 nm). The point may provide multiple sites for molecular bonds to connect. In single-molecule junction (SMJ) studies, the presence of the surrounding molecules cannot be neglected because they may affect the geometry of the SMJ, modify the excitation probability of particular molecular vibrations or influence the dielectric properties of the junction. In support of these effects, there is a spread of the measured properties when comparing different realizations of SMJs with higher or lower density of surrounding molecules. Finally, a difference can be expected regarding potential cooperative molecular reorganizations upon optical excitation between SMJs formed from well-ordered or disordered SAMs in break junctions. It is well known that contact configurations and structural rearrangement of the molecule–electrode interface occur and are why such junctions are characterized at cryogenic temperatures. These junction changes have been reviewed in detail elsewhere[139]. Throughout this Review, we assume that the junctions are static because we aim to focus on novel plasmonic–electronic properties of the junctions.

We use a classification into the three types point–point, point–plane and plane–plane junctions to provide a conceptual description of the different plasmonic modes in these architectures and experimental characterizations to confirm the origin of the modes.

Point–point junctions

Plasmon modes. Nanoscale cavities formed by two point metallic electrodes (as either lithographically patterned electrodes or nanoparticle dimers (NP dimers); see FIG. 1a) can behave as resonant plasmonic structures under external excitation (optical or electrical). These structures are often termed 'cavity'[140] and can support resonant plasmonic modes called 'localized' modes[141] as the mode profile is highly confined and well defined due to the impedance mismatch introduced by metallic surfaces, causing the cavity mode to have similar properties to a LSP mode[31]. As the contact area of point–point cavities decreases in size, from hundreds of nanometres down to tens of nanometres, the cavity mode becomes increasingly sensitive to the material properties of the electrodes, the surrounding medium, the topography at the electrode/molecule interface and, especially, the molecule embedded in the junction. Introducing molecules under an applied bias into resonant junction systems modifies the local electromagnetic environment and allows for controlled tuning of the total refractive index as well as resonant response seen by the cavity mode[142–146]. These modes of the nanocavities therefore govern the interaction of plasmons with molecules in the nanogaps.

We first discuss the primary properties of gap modes between NP dimers because of the physical similarities of nanogap modes between them and two metal tips[147–149]. NP dimers in the Mie regime (dimensions in the order of a fraction of the SPP wavelength λ_{spp}) typically support two sets of hybridized modes depending on the direction of the overall polarization[150–152]. For longitudinal polarization (FIG. 4a), the bonding dipolar plasmon (BDP) mode and the anti-BDP mode form bright and dark modes (non-radiating), respectively[153–158]. For transverse polarization (FIG. 4b), the dipoles are antiparallel in the low-energy mode and parallel in the high-energy mode and form a dark mode and a bright mode, respectively[159,160].

As the dimer gap distance decreases to an extent where quantum tunnelling of electrons becomes the dominant form of electron transport (below ~0.4 nm), a low-energy new resonant mode (charge transfer plasmon (CTP) mode) appears in the spectrum[161], characteristically marking the situation in which tunnelling electrons freely flow across the extremely small gap (FIG. 4c). A shift of the plasmon resonance frequency has been predicted in simulations and confirmed in experiments[162]. The near-field BDP red shift progressively disappears as the nanogap size decreases[163,164] and blue-shifted CTPs gradually emerge after that[37,165]. In addition to the BDP and CTP modes in point–point contact nanostructures, higher-order modes excited due to the coupling between the two 'point' nanostructures exist[166].

With molecules embedded in the gap, the tunnelling barrier will be raised or lowered depending on the electronic structure of the molecules, allowing plasmon resonances to be tuned via through-molecule tunnelling[37,47,167]. The tunnelling CTP mode with two silver nanocube plasmonic resonators bridged by SAMs was recently reported[44]. Four plasmon peaks at approximately 0.6 eV, 2.2 eV, 3.2 eV and 3.6 eV were observed by electron energy-loss spectroscopy (EELS) (FIG. 4d), which are assigned to the CTP mode (I), the BDP mode (II), the transverse corner mode (III) and the transverse edge mode (IV), respectively. By choosing aliphatic or aromatic SAMs with similar lengths in the gap, this investigation makes it possible to tune the CTP modes and to estimate the terahertz molecular conductance[142].

Another interesting effect of hybridizing the plasmonic modes in point–point junctions is the local electromagnetic field enhancement. When light directly illuminates the nanogap, the electric field in the gap is enhanced due to the high confinement of the cavity mode (FIG. 4e). The electric field enhancement E_E strongly depends on the separation of the dimers d, varying as $E_E \propto d^{-3}$ (REF.[168]). When $d \sim 1$ nm, >100 factor electric field enhancements are possible, which gives rise to high Purcell factors that stimulate efficient light–matter interactions at the nanoscale[147,169,170]. The high enhancements have also been exploited to reach several orders of magnitude enhancements of the Raman signals, thus making it possible to analyse molecular fingerprints with up to single-molecule sensitivities[171,172]. This is the driving principle behind the use of surface-enhanced Raman spectroscopy (SERS) in break junctions[32,173,174].

Characterization of plasmonic effects. NP dimer-based molecular junctions can consist of DNA[175], proteins[176,177] or molecular wires[178,179]. The major limitation of NP

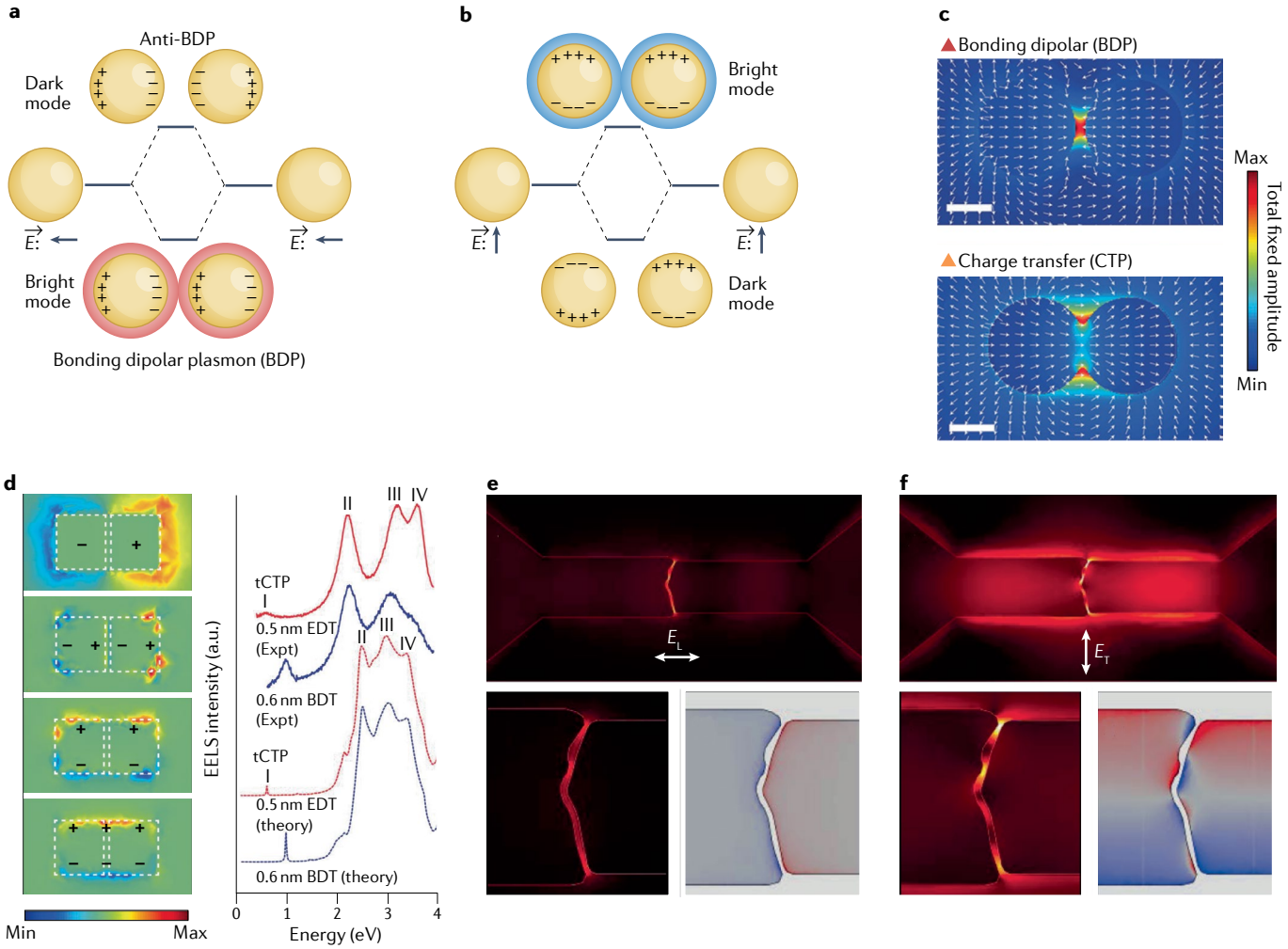

Fig. 4 | **Illustration of plasmonic modes within point–point-shaped molecular junctions. a** | Two dipolar modes with polarization parallel to the dimer axis (longitudinal). Only the low-energy mode is bright as a bonding dipolar plasmon (BDP) mode has a finite total dipole moment that an anti-BDP mode lacks. **b** | Two dipolar modes with polarization perpendicular to the dimer axis (transverse). Only the high-energy mode is bright. Reproduced with permission from REF.[151], Elsevier. **c** | Particle polarization and total field amplitude maps of the BDP mode and charge transfer plasmon (CTP) mode, with arrows indicating field directions. **d** | Measured electron energy-loss spectroscopy (EELS) spectra with the occurrence of the CTP peak and corresponding simulated maps of the electrical-field distributions for the plasmon modes. II, BDP mode; III, transverse corner mode; IV, transverse edge mode. Aliphatic EDT, 1,2-ethanedithiolate; BDT, aromatic 1,4-benzenedithiolate; tCTP, tunnelling charge transfer plasmon. **e**,**f** | Simulations of electromagnetic field enhancement (top and bottom left) and charge distribution (bottom right) upon longitudinally (**e**) and transversely (**f**) polarized light with electrical fields E_L and E_T, respectively. Panel **c** adapted with permission from REF.[161], ACS. Panel **d** adapted with permission from REF.[44], AAAS. Panels **e** and **f** are reprinted with permission from REF.[205], ACS.

dimer-based molecular junctions is that they lack electrodes, so their molecular conductance cannot be directly probed by electrical bias. The estimation of molecular conductance and the corresponding plasmon response analysis[180–182] of NP dimer-based molecular junctions are mostly achieved by far-field and near-field spectroscopic approaches such as SERS[183], absorption spectroscopy[184], optical scattering spectroscopy[185] and EELS[186–188]. In contrast, the molecular conductance as a function of V of point–point junctions can be directly explored in break junctions[14], including EBJs and MCBJs[17,189,190]. Furthermore, three-terminal devices can be formed with EBJs and MCBJs by using the substrate as a backgate electrode, which opens the possibility to shift the energy levels of the molecule inside the junctions[191–193].

Analogous to plasmonic characterization within NP dimers, the gap distance-dependent influence on the plasmon modes in other point–point junctions can also be directly characterized by EELS or UV–Vis spectroscopy and are indirectly reflected through enhanced Raman signals[194–196]. The near-field BDP red shift also progressively disappears as the nanogap size decreases in electrode-based point–point junctions, triggering the onset of a blue shift of the CTP mode. These phenomena were first studied using a form of atomic force microscopy, the oriented AFM tip to AFM tip configuration[162], and further verified by integrating two opposing bow-tie nanoantennas into MCBJ set-ups[194,197].

SERS is the second method used to analyse localized plasmonic effects, especially light polarization influence, in point–point junctions. This method does not directly

reveal possible changes of plasmon modes, because the localized strong near-fields from the plasmonic resonances in junctions are only one of the factors responsible for the enhancement effects in SERS[52]. However, SERS consistently shows its highest magnitude when the incident light is polarized along the nanogap (longitudinal) involving NP dimers[198], bow-tie nanoantennas[199], point–point junctions (MCBJs[195] or EBJs[200]) and point–plane junctions (NPoMJs[201] and STM-BJs[202]). A stronger field enhancement in transverse polarization has been recently observed in nanoparticle-based point–point junctions[203,204] and EBJs[205,206] (FIG. 4f). The latter is due to the strong dipolar plasmon mode that resonates transversely and efficiently couples with dark multipolar modes arising from subtle intrinsic asymmetries in the EBJ nanogap. This highly localized hybridized mode further gives rise to SERS enhancements and reveals the polarization dependence of SERS signals.

In contrast to these LSP effects, only very weak polarization-dependent variations of SPPs have been reported in MCBJ experiments[97,98]. This conclusion has been drawn from measuring the junction conductance while illuminating light with longitudinal and transverse polarizations on grating couplers at a relatively large distance from the junction. Possible reasons for the observed weak polarization dependence are that the junction geometry is not controlled on the atomic scale such that the polarization direction and size of the local field are not precisely controlled[196].

Point–plane junctions

Plasmon modes. Point–plane nanostructures are usually made of a metallic nanostructure or a metallic tip (as the point) that is very close to a metallic film (as the plane) and separated by a molecular layer. NPoMJs, such as nanoparticles, nanocubes, nanorods and nanodiscs, are used and are also known as nanopatch optical antennas[207], and particle on film[24]. Real nanoparticles are actually polyhedrons with a faceted surface rather than ideal spheres. Compared with realistic NP dimers, NPoMJs thus have advantages in the relative ease of fabrication and plasmon mode analysis due to the symmetry introduced by the atomically flat metal mirror. Point–plane nanostructures also include scanning-probe approaches to apply a voltage bias in STM-BJs[208–210] and AFMJs[211,212]. For the mode description of point–plane junctions, we first consider NPoMJs, and this description largely applies to other point–plane nanocavities.

The nanocavity modes are mostly confined between the bottom of the nanoparticle and the front side of the metal film (FIG. 5a). There are two different mode types: longitudinal cavity modes, which are strongly radiative and exist for all facet widths of the nanoparticle, and transverse cavity modes produced at large facets that exhibit extreme confinement[213]. As the facet width increases, the optical environment at the nanogap approaches that of a plasmonic MIM waveguide with a plane–plane junction. The difference is that the continuous MIM waveguide modes are discretized by the facet in NPoMJs. The frequency of the cavity modes spans the visible and near-infrared ranges as the MIM facet width w is varied (FIG. 5b). For different facet widths, several cavity modes appear, denoted by (mn), based on spherical harmonics, where $l = 0, 1, 2, \ldots$ and $-l \leq m \leq l$ (REFS.[23,214]). The properties of the (mn) mode and its spectral position, coupling and field enhancement are closely related to the gap space. The most dominant modes observed in experiments are modes with even m (for example, the (02) mode) that possess a strong out-of-plane optical field in the nanogap. Dark-field scattering spectroscopy typically reveals that these even modes have resonances in the visible to near-infrared region (FIG. 5c) and are dependent on the gap size set by the height of the SAM, the nanoparticle facet width, and the refractive index of the surrounding medium. There are also non-radiative odd m modes that support in-plane optical fields in the near infrared and are dominant for larger gaps. The strongly confined nanocavity modes out-couple through plasmonic antenna modes l_k with a symmetry that matches the cavity modes, yielding a mixed-mode j_n. For a more detailed review of the NPoMJ modes and antennas, see REF.[23].

An important question is how the cavity mode interacts spatially with the SAM in the near field of the plasmonic nanocavity. The mixed modes display distinctive properties in near-field and far-field detection. It is important to note that the mixed mode couples to SAMs in the near field within the gap, whereas far-field radiation of these modes is driven by oscillating charges on the top surface of the nano-object. By accounting for the open and dissipative nature of the plasmonic nanocavity, it is possible to obtain natural resonant quasi-normal modes of the system, in contrast to normal modes that typically describe other photonic systems[215–217]. Quasi-normal decomposition is useful to obtain many more spatial and spectral properties of the cavity modes[214].

Fig. 5 | **Illustration of plasmonic modes and scattering spectra within molecular junctions in point–plane junctions. a** | A gold nanoparticle on mirror molecular junction (NPoMJ) with nanogap index n_{gap}, background index n_b and facet width w. **b** | Gap mode S_{mn} tuning with facet width w in a flat-junction NPoMJ. **c** | Dark-field scattering spectra with different molecular spacers. **d** | Near-field spatial distribution of different S_{mn} cavity modes. **e** | Spatial distribution of the electric field with radially polarized light (top) and linearly polarized light (below). **f** | Temperature dependence of dark-field scattering. **g** | The full width at half-maximum (FWHM) of the scattering spectra in panel **f** versus temperature. **h** | Simulated scattering spectra of NPoMJs with molecular bridges of different conductance values in the gap and the corresponding occurrence of higher-order charge transfer plasmon (CTP). Peak I corresponds to the higher-order BDP mode; peak II to the higher-order CTP mode; and peak III to the BDP mode. BPT, biphenyl-4-thiol; BPDT, biphenyl-4,4′-dithiol; G_0, conductance quantum; MIM, metal–insulator–metal. Schematic of surface interaction at the bottom of panel **a** and plot in panel **b** adapted with permission from REF.[23], Springer Nature Limited. Schematic of gold nanoparticle on mirror in panel **a**, and panel **d** adapted with permission from REF.[214], ACS. Plots in panels **c** and **h** were adapted with permission from REF.[223], ACS. Panel **e** adapted from REF.[218], Springer Nature Limited. Panels **f** and **g** were reprinted from REF.[220], CC BY 4.0 (https://creativecommons.org/licenses/by/4.0/).

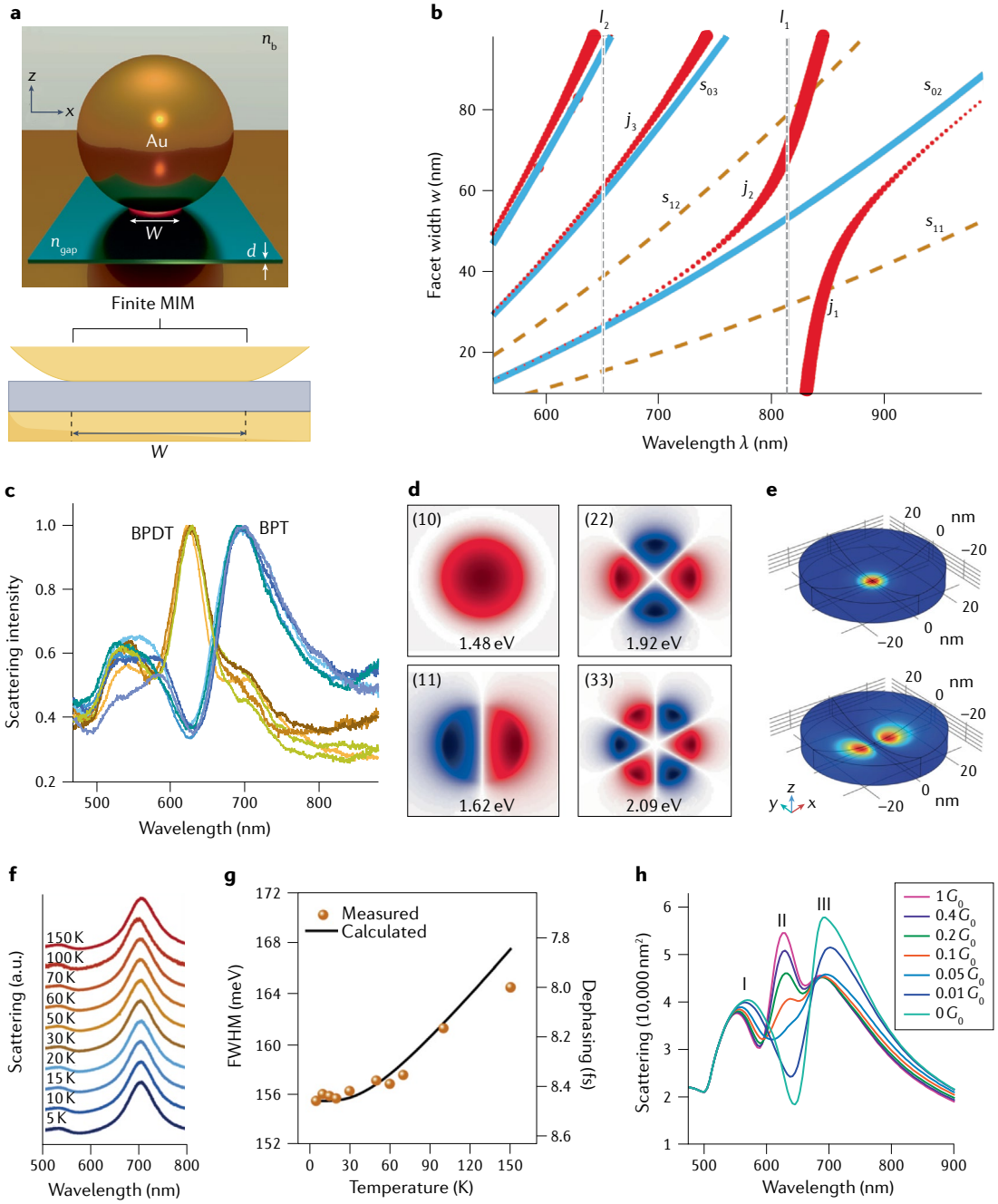

In the near field, the (10) mode has a spatial distribution that looks similar to a spot, and the (11) mode has two lobes with a node in the centre (FIG. 5d). The out-of-plane modes can be excited using a vertical (*z*-axis) component of a plane wave and even more efficiently using a radially polarized beam[218] (FIG. 5e), in contrast to the in-plane modes that are excited by a horizontally polarized plane wave. The far-field radiation patterns of the in-plane and out-of-plane modes radiate close to normal and predominately at high angles (>50°), respectively, indicating a significant difference in the dipole emission properties of the modes. Therefore, a complete characterization of the cavity modes is a combined observation of dark-field scattering spectra and far-field imaging of the radiation pattern[219].

There have been many efforts to tune these plasmonic modes by taking advantage of the sensitivity of the modes to different parameters, as mentioned above, which are reflected by the line width and line shape of scattering spectra. The line width (which quantifies the plasmon damping) of the (10) mode shows low sensitivity to temperature and decreases by a few per cent over a wide temperature range of more than 100 K[220] (FIG. 5f,g). This insensitivity to temperature is a consequence of the fact that temperature-independent processes, such as electron–electron scattering and electron–surface scattering, are dominating. In the given examples they contribute by up to 64% of the scattering, as revealed by full-wave electromagnetic calculations. The resulting slight line width decrease results from the temperature-dependent

electron–phonon scattering. The observed changes in the dark-field scattered spectrum are attributed to plasmonic effects. However, it is well known that molecular layers have phase transitions, or changes in temperature may cause disorder, which affects tunnelling currents across monolayers[221,222]. It is therefore an interesting challenge to probe changes to the molecular layers inside a plasmonic nanocavity with respect to temperature changes and whether such changes affect the optical properties of junctions. In addition, the nanocavity resonance controlling the nanogap conductance by using SAMs of almost equivalent length (biphenyl-4-thiol (BPT) and biphenyl-4,4′-dithiol (BPDT)) but differing molecular bonds gives 50-nm blue shifts of the (10) mode[185]. Furthermore, a clear higher-order CTP mode (similar to point–point junctions) emerges in the BPDT-bridged gold nanoplate–gold nanoparticle (AuNP) heterodimers, which unravels the nature of the emergent plasmon modes with electron transport behaviour in molecular junctions[140,223]. The simulated scattering spectra with different bridging SAMs in the junctions reveal that the intensity of the higher-order BDP mode (peak I in FIG. 5h) and the depth of a second peak featuring an asymmetric Fano line shape[224–226] are both greatly reduced when the molecular conductance G is increased gradually from $0G_0$ to $0.05G_0$ (where G_0 is the conductance quantum). As the junction conductance is further increased from $0.05G_0$ to $1G_0$, this higher-order BDP mode (specifically the bonding dipole–quadrupole mode) slightly blue-shifts and decreases in intensity. At the same time, a higher-order CTP mode emerges (peak II) at the high-energy side of the BDP mode (peak III), exhibiting a prominent increase in intensity with increased molecular conductance.

Characterization of plasmonic effects. One of the most common methods to simultaneously study plasmonic phenomena and molecular conductance in point–plane junctions is using STM-BJs. Exchanging one nanoparticle electrode for a scanning tip reduces the radiative emission because the aforementioned nanoparticle antenna modes are shorted out by the high conductance of the tip[227]. Although, due to their relatively large size, the resonances of STM tips are typically in the microwave range[228], this resonance range is equivalent to acting as a mere resistor from an electrical circuit point of view, and the STM tip can still act as a boundary of a cavity[208,229,230]. However, the out-coupling efficiency of a scanning tip is much lower than that of a large nanoparticle. The out-coupling can be enhanced by attaching a nanoparticle to the tip to have the advantages of both structures[231,232] or by introducing gratings on the tip or substrates[233,234]. Here we discuss the more general cases in STM-BJ nanocavities[235–237]; the spatial tunability to perform more flexible conductance measurements is introduced while the nanocavity modes are also maintained. The high Purcell factor in the order of 10^5–10^6 and high quantum efficiency (~40%) allows SAMs in STM-BJ nanocavities to emit light more efficiently, relative to the emission in free space[43,238]. The photon emitting frequency and intensity depend on molecular states involving inelastic tunnelling channels[239,240], the chemical structure of the molecular emitting units[241], the thickness of the insulator separating SAM layer from the lower gold substrate[242], the bias voltage magnitude and the polarity[239,243–245].

Fig. 6 | **Typical plasmon excitation or detection by tunnelling electrons in STM-BJs. a–c** | There are three different tip positions from the single zinc-phthalocyanine (ZnPc) molecule and corresponding scanning tunnelling microscope-induced luminescence (STML) spectra. The tip position is far from the molecule (panel **a**), near the molecule (panel **b**) and right on top of the molecule (panel **c**). E_e is the energy level of the excited state; E_g is the energy level of the ground state. A typical Fano-shaped spectra is observed in panel b due to the interaction between the nanocavity plasmon mode and the two-level emitter in close proximity. The thin sodium chloride (NaCl) spacer layers between ZnPc and the silver (100) substrate work as a decoupling layer for suppressing the fluorescence quenching and yield molecule-specific electroluminescence. **d** | Experimental set-up and strategy to map hot-carrier energy distributions. Surface plasmon polaritons (SPPs) are excited by illuminating the grating coupler several micrometres away from the biased gold STM break junctions. Inset shows an SEM image of the corresponding grating coupler. V_{bias} is the voltage applied between the STM tip and the substrate. **e** | Current and conductance histograms of the scanning tunnelling microscope break junction (STM-BJ) shown in panel **d** obtained from more than 2,000 traces for dark (grey) and SPP-excited (magenta) measured at $V_{bias} = 0.1$ V. Inset shows representative conductance traces following the same colour coding. G_0 is the conductance quantum. **f** | Normalized electric field distribution of the STM tip cavity shaped with a groove on the shaft, plotted on a logarithmic scale simulated for $L = 3$ μm at 610 nm. **g** | STML spectra measured over the silver (111) surface utilizing gold tips with grooves located at $L = 3$, 6 and 10 μm ($V_{bias} = 2.5$ V, $I_t = 9$ nA). L is the distance between the groove edge and the STM tip apex. Panels **a**,**b** and **c** are reprinted from REF.[247], CC BY 4.0 (https://creativecommons.org/licenses/by/4.0/). Panels **d** and **e** are adapted with permission from REF.[234], AAAS. Panels **f** and **g** are reprinted from REF.[233], CC BY 4.0 (https://creativecommons.org/licenses/by/4.0/).

The corresponding spectral shape, peak position and width of the emission are determined by the interaction of the discrete energy states of a single molecule and the continuum-like state of the plasmonic nanocavity[246]. For example, FIG. 6a–c shows that when the STM tip is close to a single zinc-phthalocyanine (ZnPc) molecule, the STM luminescence (STML) spectrum exhibits a clear Fano dip (FIG. 6b) superimposed over the original broad plasmonic spectrum[247] (FIG. 6a). The Fano dip deepens and widens as the tip approaches the molecule before directly being positioned above the molecule, indicating an increase in the coupling strength between the nanocavity plasmon mode and the ZnPc molecule (FIG. 6c).

The modification of the geometry of the STM tip or introducing structures, such as gratings, onto the plane substrate is an effective tool to reflect the SPP/LSP effect on electron transport in SMJs. FIGURE 6d shows a junction based on a SAM supported by gold in contact with a STM tip in proximity to a grating coupler[234]. In this configuration, single-molecule conductance could be measured and used to quantify the

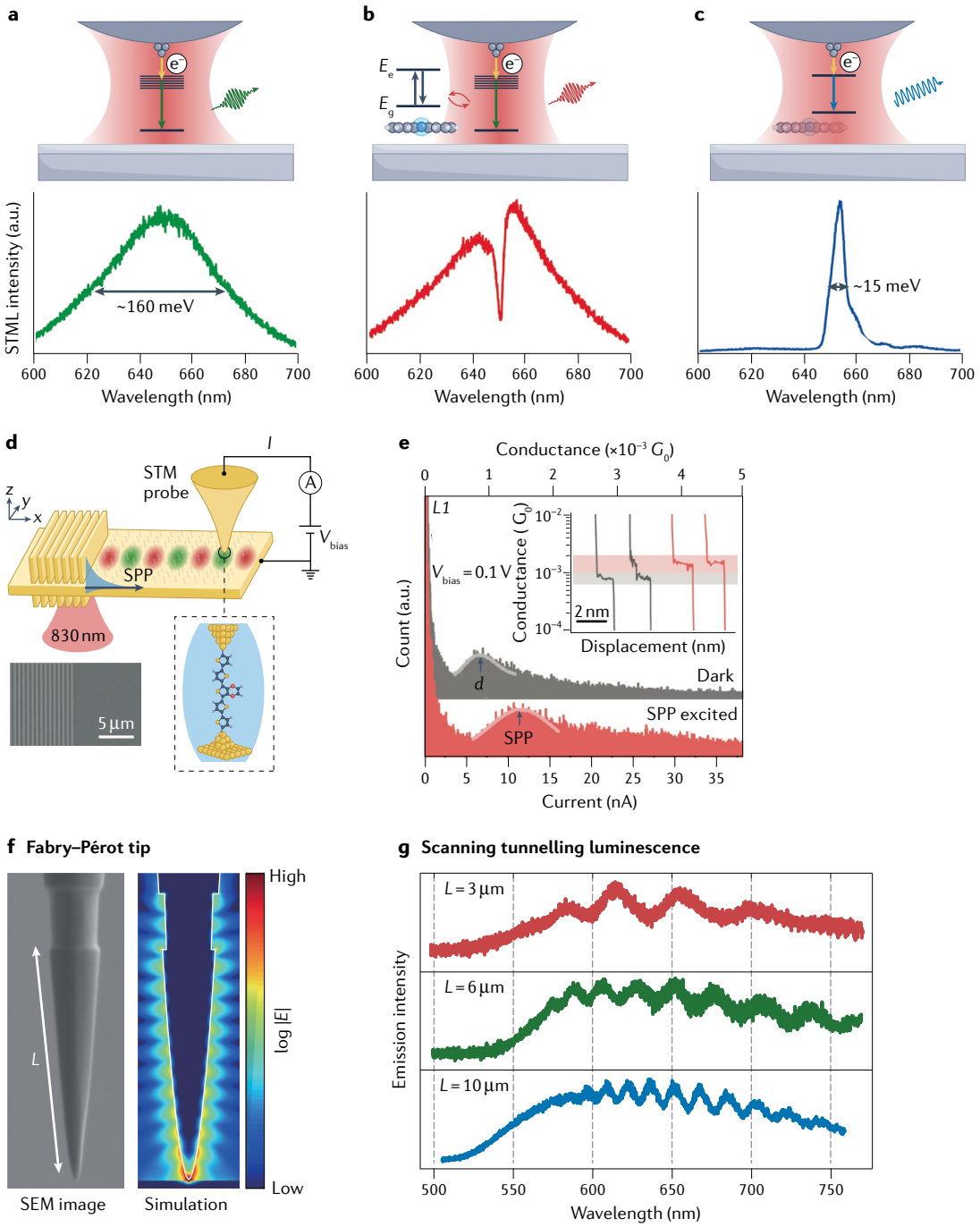

steady-state energy distributions of hot electrons (due to the non-radiative decay of surface plasmons) with and without plasmonic action as a function of V (FIG. 6e). The measured hot electron-induced current originates from symmetric modes supported by the symmetric dielectric environment. The most probable additional hot electron-induced current shown in statistical histograms is in the order of several nanoamperes. The value thus depends on the gold film thickness and the tip position relative to the grating edge. FIGURE 6f shows that a groove on the shaft of the STM tip results in interference between the LSP in the junction and the propagating SPP reflected to the apex. This groove modulates the STML spectra, exhibiting a periodic oscillation in this near-field spectral response[233,248] (FIG. 6g). In this case, the modulation of LSP interference with SPP also contributes to the tautomerization of single porphycene junctions.

Another recently observed phenomenon in point–plane nanojunctions is spectral and temporal fluctuations of SERS peaks from molecules in the junctions. The dynamics indicate bursts of new SERS peaks that often appear on both the Stokes and anti-Stokes sides (FIG. 7a). This type of behaviour has been observed in several systems and configurations, including NPoMJs[249,250] and even individual nanostructures[251]. Tremendous efforts have been made to resolve the fast dynamics that require acquisition rates approaching a million frames per second[252–254]. Using a single-pixel detector to measure

a certain SERS peak, the intense burst of intensity lasts for only a few tens of microseconds. It is interesting that this kind of dynamics is similar to the blinking effect that has been observed in single-molecule spectroscopy[255,256]. The spectrally resolved time dynamics indicate a major difference with spectral shifts of SERS peaks of 30 cm^{-1} within 3 ms, which indicate molecular conformation changes[254]. Furthermore, fluctuations in broadband photoluminescence emission[257] (instead of SERS peaks) have been observed (FIG. 7b), and the frequency of occurrence of these events depends on the flexibility of the molecular backbone[258,259]. To understand these observations, density functional theory calculations show that an adatom close to a single molecular bond is sufficient to break Raman selection rules due to high field gradients, which gives rise to new SERS peaks[260]. The adatom can confine electric fields $V_{eff} < 1\ nm^3$, hence the name picocavity (FIG. 7c). The ultra-small localization of light with picocavities excites specific molecular bonds. It selectively amplifies some vibrational modes of trapped molecules, thus demonstrating the possibility of resolving the dynamics of individual bonds within molecules[249,261]. The broadband transient emission (also termed flares) is attributed to localized defects that perturb the gold crystal structure, and the defects migrate more rapidly than typical adatom diffusion. These defect states are mainly formed between crystalline domains, allowing them to adopt different nanodomains and nanoshapes[258] (FIG. 7c). A detailed understanding of the mechanism and forces that activate the picocavities and flares is still lacking. Moreover, being able to activate and stabilize these events for several minutes or even hours in a controlled manner would be useful, as this is necessary for possible applications of picocavity and flare modes in catalysis and sensing.

Regarding molecular emitters inside a point–plane geometry, 1–10 precisely positioned methylene blue molecules were used to obtain a Purcell factor as high

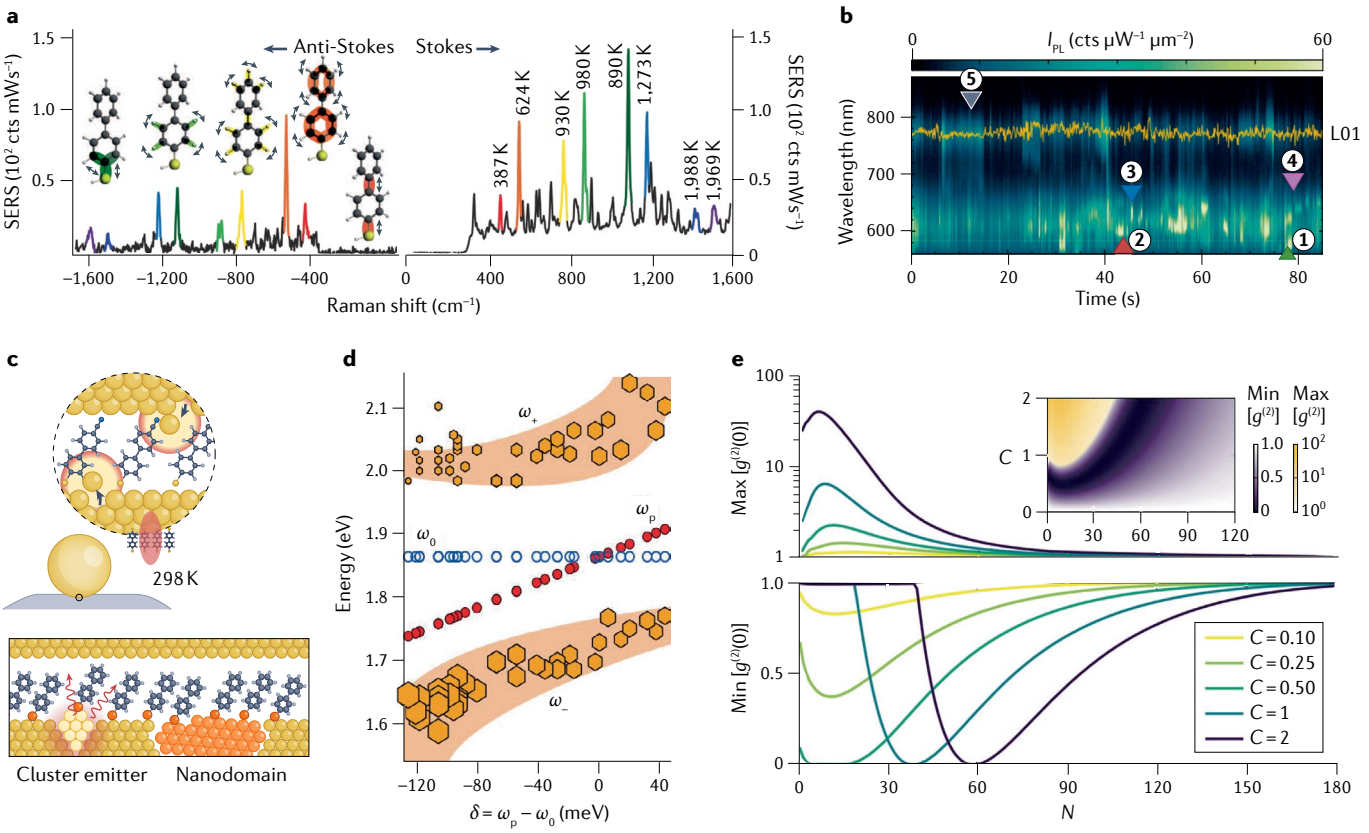

Fig. 7 | **Measurements of different molecular–plasmon coupling schemes in plasmonic nanocavities. a** | Surface-enhanced Raman spectroscopy (SERS) spectra from biphenyl-4-thiol (BPT) molecules in picocavities. Anti-Stokes/Stokes spectra at the same time whereas colour indicates isogenesis picocavity-induced lines. Vibrational eigenmodes and effective temperatures also shown. **b** | Time series of plasmon-enhanced photoluminescence from BPT in a plasmonic nanojunction. Arrows indicate individual emissions that deviate from the typical baseline emissions. **c** | Possible interpretations of the spectral fluctuations. Upper panel: an adatom is pulled out from the gold surface and localizes the electric field to break the Raman selection rules. Lower panel: nanoclusters or nanodomains are formed under laser irradiation to result in metallic transient emission. **d** | Resonant energies of methylene blue (MB) exciton (ω_0), plasmon (ω_p) and hybrid (ω_+ and ω_-) modes as a function of extracted detuning $\delta = \omega_p - \omega_0$. **e** | Maximum (top) and minimum (bottom) correlation functions as functions of the number of emitters (*N*) for several values of the single emitter cooperativity C. Inset in upper panel shows the map of photon positive (yellow) and negative (violet) correlations as functions of *N* and *C*. Panel **a** is reprinted with permission from REF.[250], AAAS. Panel **b** is reprinted from REF.[259], CC BY 4.0 (https://creativecommons.org/licenses/by/4.0/). The top part of the schematic in panel **c** is adapted with permission from REF.[249], ACS. The bottom part of the schematic in panel **c** is adapted from REF.[259], CC BY 4.0 (https://creativecommons.org/licenses/by/4.0/). Panel **d** reprinted with permission from REF.[43], Springer Nature Limited. Panel **e** is reprinted from REF.[269], CC BY 4.0 (https://creativecommons.org/licenses/by/4.0/).

as 3.5×10^6 at room temperature under ambient conditions[43]. The two spectral peaks (ω_+ and ω_-; shown in FIG. 7d) indicate that a Rabi frequency $g = 380$ meV is yielded when the dye molecule's dipole moment is perfectly aligned with the gap plasmon, leading to strong coupling between a single optical emitter and the cavity. They also introduced a straightforward non-invasive approach by using DNA origami as a scaffold to pin different functional elements so that precise positioning of a single-dye molecule at the centre of the gap can be achieved and Rabi splitting (~ 80 meV) in the strong-coupling regime is observed[260,262].

Achieving the strong-coupling regime requires increased coupling strength g, suppressed emitter decay rate γ and suppressed cavity loss rate γ_C. For cryogenic emitters, the suppressed emitter decay rate γ enables reaching strong coupling for large cavities formed by whispering gallery spheres, microdiscs, photonic crystals or micropillars. For room-temperature devices, typical decay rates for embedded dipoles are $\gamma \sim k_B T$, and the coupling strength g is proportional to $1/\sqrt{V_{eff}}$ based on Eq. (6). Thus, the quality factor $Q \sim 10$ requires cavities with $V_{eff}/V_\lambda < 10^{-5}$, where $V_\lambda = (\lambda/n)^3$ at wavelength λ and refractive index n. This coupling contributes to the investigation of individual chemical events[263,264], making it possible to uncover information on single-molecule reaction kinetics and ultra-sensitive biosensing[265].

Remarkably, a single emitter in this plasmonic nanocavity does not quench despite the close proximity of the dye to metal surfaces, and optical emission from every single emitter can be enhanced by $>10^3$ (REFS.[266,267]). The suppression of quenching is as a result of the enhanced radiative decay rate due to the high Purcell factor in the nanocavity whereas the non-radiative decay rate is also enhanced owing to the close proximity of the metal surfaces. This interplay of both decay rates in the nanocavity combines to give a quantum efficiency of up to ~40% compared with <0.1% for a single nanoparticle. Thus, the emission of a weak emitter with a low quantum yield (<0.1%) is greatly enhanced, despite the vicinity of the metal surfaces. However, quenching sets in when the nanogap distance is less than 0.4 nm, where non-radiative decay dominates[268]. Experimental and theoretical investigations have demonstrated complex changes in the photon statistics of emission from plasmonic nanocavities as a function of cavity detuning, excitation wavelength and several emitters[262,269,270] (FIG. 7e). These studies demonstrated both photon bunching and photon anti-bunching, including the photon blockade effect, which results from destructive interference processes, also called unconventional anti-bunching. The findings demonstrate the feasibility of the realization of nanoscale non-classical light sources operating at room temperature in plasmonic nanocavities[271].

Plane–plane junctions

Plasmon modes. Plane–plane junctions have different plasmonic behaviour to point–point and point–plane junctions according to their dimensions. Above a certain lateral junction size, the cavity mode transitions from resonant to non-resonant[272,273]. Here, the metal attenuates the mode before it reflects off the impedance mismatch at the junction edges so that it no longer has cavity-like behaviour but, instead, behaves similar to a highly confined SPP[39,274–276]. These systems then act as MIM waveguides, supporting confined SPP modes according to the thickness and dielectric constants of the metal and the insulator. The transition happens when the lateral junction size overcomes the confined SPP propagation length in this MIM configuration. These systems are relatively inert to nanoscale changes in the device geometry, and this insensitivity can be exploited for SPP waveguiding and out-coupling[277,278]. As the insulator thickness is given by the SAM height, the SPP mode exhibits odd symmetry of E in the direction of the horizontal plane (longitudinal component), but the damping of the propagating mode increases, resulting in a much shorter propagation length[279]. In practice, the supported modes in these junctions are much more complicated due to the surface roughness of the electrodes[39,40] and the conformational dynamics of SAMs[280], as in point–point junctions. At variance to the point–point contacts, in the plane–plane contacts there are many LSPs with different frequencies, which increases the apparent spectral width.

Characterization of plasmonic effects. Due to the requirement of good contact between the SAM and the electrodes over the large contact area in plane–plane junctions, soft conducting layers are introduced to protect the molecular layer to improve the rate of working junctions. Electrochemical deposition-based molecular junctions[281–283], PEDOT:PSS (poly-(3,4-ethylenedioxythiophene) stabilized with poly-(4-styrenesulfonic acid))[284,285], graphene[286] or the usage of liquid metals (EGaIn/Ga_2O_3 (REF.[287])) as the top contact have been instrumental for the progress of large-area molecular junctions recently (FIG. 8a–c). Owing to the transparent thin carbon layers in carbon-based STJs, it is possible to characterize their photocurrent spectrum by internal photoemission. The internal photoemission spectrum contains information on the relative positions of the frontier orbitals and the electrode Fermi level in the molecular junction, with signs of the photocurrent indicating whether LUMO or HOMO mediates in electron transport[288].

STJs were formed with EGaIn/Ga_2O_3 as the top electrode together with an ultra-flat gold bottom substrate to build plane–plane plasmon sources[289] (FIG. 8c). Inelastic tunnelling charge carriers excite LSPs inside the STJ area and SPPs at the edge of the STJs along the gold–SAM–air or gold–SAM–PDMS interface. LSP emission and SPP leakage radiation were recorded by real-plane and back focal-plane imaging (FIG. 8d,e), revealing two particular properties of molecular electronic plasmon sources based on STJs[280,290]. On the one hand, the blinking of the molecular electronic plasmon sources was characterized by the 'on' and 'off' periods, originating from conformational dynamics of the molecules. The blinking followed a power-law relation between the probability density and time of the 'on' and 'off' periods and presented distinct characteristic frequencies in power spectral density analysis. The blinking rates were well controlled by the rigidity of the molecular backbone so that molecular junctions

Internal photoemission
Unlike external photoemission, the photoenergy of the internal photoemission process is lower than the electrodes' work function but high enough to lead to a measurable current across the junction.

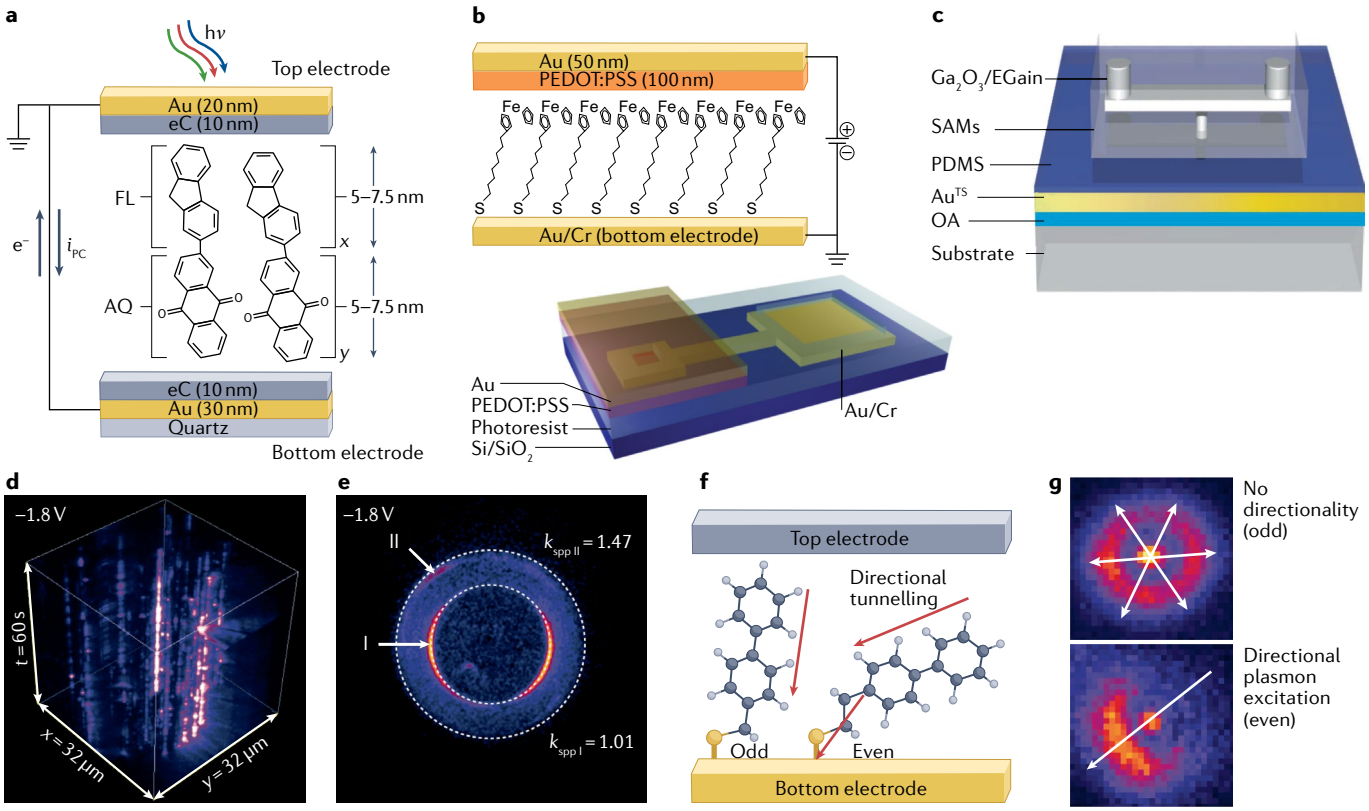

Fig. 8 | **Typical structures and plasmon excitation in STJs. a** | An Au/eC/AQ/FL/eC/Au self-assembled monolayer (SAM)-based tunnelling junction (STJ) structure. eC denotes electron beam–deposited carbon. **b** | Structure of large-area STJ. **c** | The STJ with the Ga_2O_3/EGaIn (eutectic gallium and indium alloy) top electrode constrained in polydimethylsiloxane (PDMS) and an ultra-flat gold bottom electrode obtained by template stripping (TS) supporting the SAM. An optical adhesive (OA) was utilized to glue the glass support on the gold to facilitate TS. **d**,**e** | Blinking of plasmon sources in the real plane (panel **d**) and the back focal plane (panel **e**), which is excited in an STJ with an SC_{12} SAM on a 50 nm gold film measured at $V = -1.8$ V. Modes I and II in panel **e**, respectively, indicate surface plasmon polariton (SPP) modes with normalized wavevector $k = 1.01$ and $k = 1.47$, where the normalized wavevector $k = k_{spp}(\omega)/k_0(\omega)$, k_{spp} is the wavevector of the SPPs and k_0 is the wavevector of light in free space. **f** | Representation of the orientation of the biphenyl (BPh) unit on gold with an odd and even number of $(CH_2)_n$ units for $n = 1–2$. Red arrows indicate the direction of the tunnelling electrons defined by the tilt angle of the BPh unit. **g** | White arrows in the defocused images indicate no directionality with odd CH_2 units and directional SPP launching with even CH_2 units.PEDOT:PSS, poly-(3,4-ethylenedioxythiophene) stabilized with poly-(4-styrenesulfonic acid). Panel **a** reprinted with permission from REF.[331], Wiley. Panel **b** adapted with permission from REF.[285], Wiley. Panels **c**,**d** and **e** are reprinted from REF.[289], Springer Nature Limited. Panels **f** and **g** are adapted with permission from REF.[291], ACS.

with flexible aliphatic molecules blink and junctions with rigid aromatic molecules do not[290].

On the other hand, the dipolar emission of the molecular electronic plasmon sources was characterized by defocused real-plane images. The dipolar emission direction was found to follow the tilt angle of the SAM molecules, which defines the tunnelling direction of the charge carriers. By changing the functional groups of the molecules, the dipolar emission direction was controlled by the tilt angle of (and the tunnelling direction through) the functional groups (FIG. 8f,g), resulting in well-defined directional excitation of SPPs[235,291]. Molecular electronic plasmon sources based on such STJs may realize new applications by introducing more types of molecular functions, and their mechanism of SPP excitation and excitation efficiencies may also be further improved.

The authors proposed that this blinking originates from conformational dynamics of the molecules where inelastic tunnelling events excite vibrational states of the molecules: molecules in an extended conformation can make good electrical contact with both electrodes supporting large tunnelling currents (and, consequently, more SPPs are excited), in contrast to molecules in a folded conformation. The blinking rates depend on the applied bias and rigidity of the molecular backbone, which supports this interpretation. These observed electrically driven dynamics might have some similarities with the spectral dynamics in plasmonic nanocavities that are attributed to the movement of gold adatoms and structural changes (see section "Characterization of plasmonic effects" for point–plane junctions). However, whether the influence of adatoms and structural changes is also important in electrically driven tunnel junctions remains an open question. It is also unclear whether these observations are related and whether they can be controlled.

Applications

Applications of the interplay of plasmons with molecular junctions cover the aspects of switching, sensing, trapping and energy harvesting (FIG. 9), and are taking

advantage of the various junction architectures and phenomena described in the previous sections.

Plasmonic molecular switches

Molecular conductance switching in plasmonic junctions mostly arises from the photocurrent enhancement upon PAT or hot electrons. The current enhancement induced by field enhancement has been reported in suspended wire molecular junctions[38,63,292], squeezable break junctions with the combination of an underneath Kretschmann configuration and a bendable top electrode[64], tip-enhanced Raman spectroscopic junctions[48], AFMJs[293] and STM-BJs[58,234], among others. The optical voltage V_{opt} in 1-octanethiol suspended wire molecular junctions was estimated to be 1.26 V nm^{-1} with the laser power of 6.5 mW μm^{-2} and the wavelength of 658 nm (1.89 eV)[38]. Correspondingly, V_{opt} in 2,7-diaminofluorene (DAF) squeezable break junctions was determined to be 0.169 V with the laser power of 1.56 μW μm^{-2} and the wavelength of 781 nm (1.59 eV)[64]. Current contributions (in the dimension of tens of picoamperes) due to hot-electron transport have also been reported in a network array of molecularly linked AuNP-based junctions[294]. In FIG. 9 we illustrate selected representative examples.

Molecular conductance switching upon illumination in NPoMJs was used to build optically accessible electronic devices in a crossbar geometry[65] (FIG. 9a). In that realization, the creation of a voltage V_{opt} around 30 mV in NPoMJs from 100 μW incident light ($\lambda = 633$ nm) generates a photocurrent beyond 10 nA mW^{-1} by optical rectification. Moreover, a positive conductance switching from off to on under irradiation with a specific wavelength in junctions was observed by embedding a one-dimensional AuNP chain into a conductive polymer polypyrrole (PPy) nanowire[295]. Under the illumination with 530 nm wavelength and 0.3 mW cm^{-2}, an additional current contribution of 40 pA can be added on top of the initial dark current of 55 pA. Complementary, negative conductance switching from on to off was obtained when small PEDOT nanowires bridge an ultra-microelectrode and AuNPs attached to an indium tin oxide (ITO) substrate immersed in an electrolyte[296] (FIG. 9b). An on/off conductance ratio higher than 1,000 was achieved with the current decreasing from 2 μA to 2 nA under white light illumination. The former repeatable current switching was attributed to optical rectification, and the latter was attributed to the transfer of hot electrons from the AuNPs towards the contacted PEDOT nanowires which result in the reduction of the small part of the bridge.

Plasmonic molecular sensing

The strong field enhancement in plasmonic nanostructures amplifies molecular signals in junctions for sensing applications. Different spectroscopic and charge transport approaches have been implemented to study dynamic processes or chemical reactions[297–299]. Examples include combinations of molecular conductance characterization, SERS with molecular junctions[183], dark-field along with optical scattering spectra[185] and EELS analysis[44]. However, the reproducible and controlled preparation of highly uniform plasmonic molecular junctions for applications ranging from molecular detection to stable single-molecule sensing still remains challenging.

The key elements to achieve highly sensitive sensing and homogeneous plasmon line widths in plasmonic molecular junctions are strongly reduced interaction volumes and narrow size distribution of the nanoelectrodes[297]. The plasmonic architectures increase the excitation rate, enhance the emission intensity and modify the quantum yield of target molecules, which can amplify small changes of real-time single-molecule chemical reaction events in SERS applications. For instance, the discretized intensities of SERS peaks reflect individual events of the formation of DMAB via different reaction pathways[263] (FIG. 9c). With a similar NPoMJ configuration, hot electron-induced redox processes in a series of different aromatic molecules with corresponding SERS spectroscopy have also been analysed[297]. In diagnosis applications, fluorescently labelled biomolecular sensing in microchannels is based on the diffusion of plasmonic nano-objects, and counting the photons in the resulting fluorescence bursting (FIG. 9d). By analysing the bursts in contrast to unenhanced molecules, information on the analyte concentration can be deduced[300–302]. Another approach to sensing is to detect the shift of the LSP resonance in the extinction and scattering spectra when receptors functionalized on the sensor surface combine with ligands for analyte detection. Single-particle scattering spectra have been recorded using a dark-field microscope. Despite their broad line width and the minute shift, concentration-dependent plasmon shifts of a few nanometres were observed when monitoring streptavidin binding to biotin-functionalized nanoparticles[303]. The relative ease of the sample fabrication presents an advantage compared with techniques that offer higher sensitivity but are more involved, such as using line gratings[304]. For interested readers, REFS.[305–307] are specialized review articles that have systematically summarized the applications of plasmonic molecular detection.

Plasmonic molecular trapping

Plasmonic gaps provide a powerful tool in near-field trapping of molecules and nanoparticles, well beyond the diffraction limit of far-field light[308]. As the optical gradient force rapidly decreases with the third power of the nano-object size ($\sim r^3$), far-field light fails to trap single small molecules at ~10 nm[309]. Recently, plasmonic biomolecules trapped into the gap position at gold surfaces or silver nanoaggregates have been employed together with SERS measurements[310,311]. By switching the laser illumination on and off, DNA was displaced stepwise through a nanopore that was in the gap of a point–point bow-tie junction[312].

As plasmonic near-field intensities are up to three orders of magnitude higher than the respective far-field intensities, these can significantly improve the capturing efficiency and thus, in principle, highly increase the probability of single-molecule trapping within the plasmonic junctions. Stable and direct spatial control over a single molecule in a fixed plasmonic nanogap remains challenging because the radiation pressure is too small to overcome the thermal fluctuation energy below nanogap sizes of 1–3 nm. But by adjusting the nanogap width

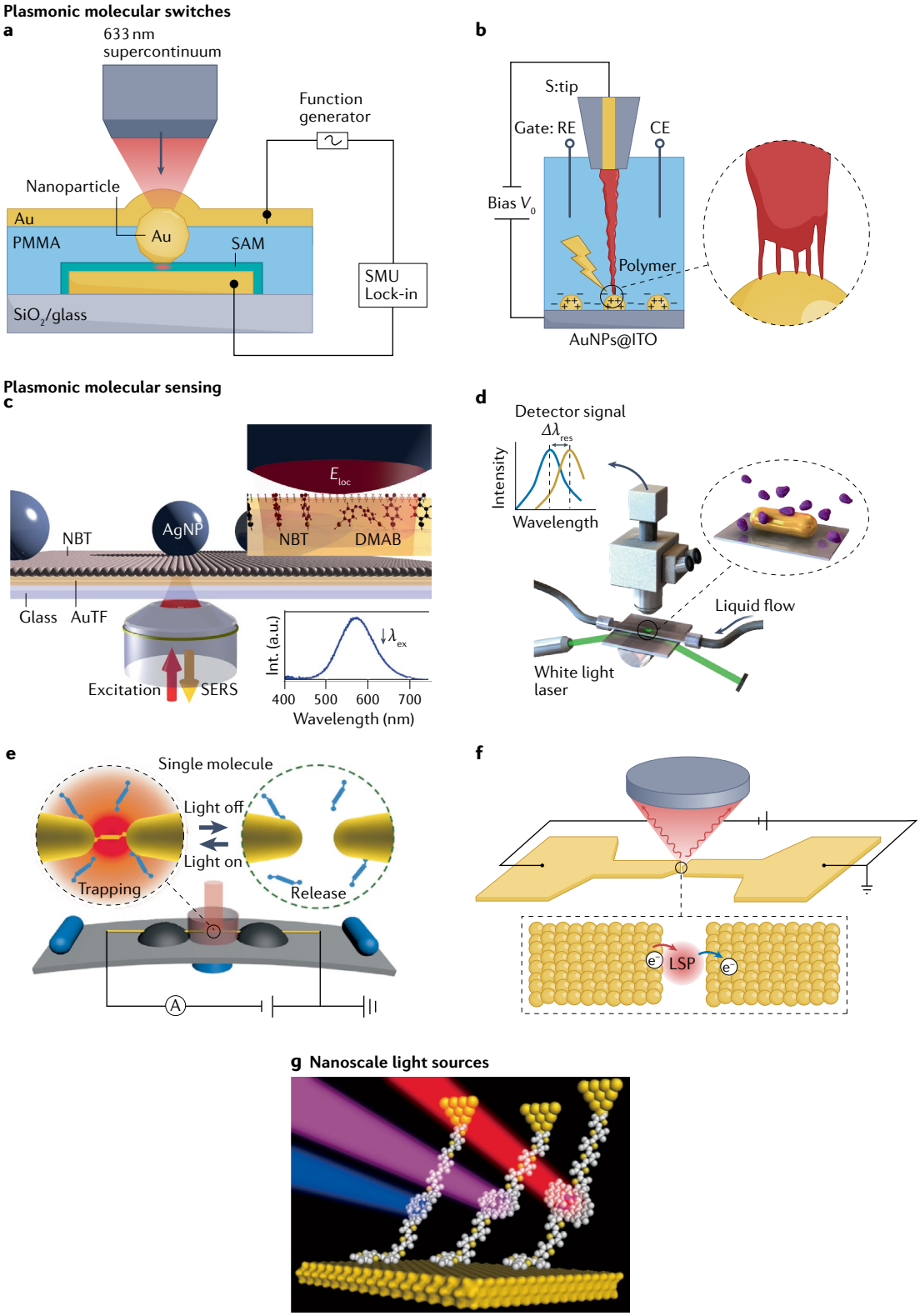

in MCBJs, direct trapping and release of single molecules at room temperature has been achieved[313] (FIG. 9e). Wavelength-controlled optical forces were found to increase the formation probability of molecular junctions, as monitored by the analysis of the conductance histograms when using model molecules that do not react to light, such as 1,4-bis((4-(methylthio)phenyl) ethynyl) benzene) (OPE3-SMe). A much prolonged lifetime of molecular junctions has also been seen in STM-BJs (FIG. 9g). In STM-BJs with a single 1,4-benzendithiol (BDT) molecule, a moderate incident light intensity of 11 mW μm^{-2} results in a >10-fold increase in minimum lifetime compared with laser-OFF conditions[314]. This plasmonic near-field trapping offers a new strategy to

◀ Fig. 9 | **Selected examples of applications of plasmonic devices. a** | Representations of plasmonic switches in a nanoparticle on mirror molecular junction (NPoMJ) forming a nanocavity, contacted to PMMA insulating layer and semi-transparent top gold electrode. **b** | AuNPs on indium tin oxide (ITO) with a PEDOT bridge in the electrochemical set-up. One or a few nanoparticles are in contact with a few nanowires and control the transport properties of the whole device. **c** | Illustration of a AgNP–DMAB–AuTF junction and simultaneous surface-enhanced Raman spectroscopy (SERS) trajectory of 4,4′-dimercaptoazobenzene (DMAB). **d** | Experimental set-up and sensing time-resolved single protein attachment events through plasmonic wavelength shifting. **e** | Single-molecule plasmonic optical trapping achieved by mechanically controllable break junctions (MCBJs) under laser irradiation. **f** | Light emission in electrically driven tunnel junctions, where localized surface plasmon (LSP) is excited by the inelastic tunnelling electrons. **g** | Illustration of controlling the light emission colour of scanning tunnelling microscope break junctions (STM-BJs) with three different emitting porphyrin derivatives. AgNP, silver nanoparticle; CE, counter electrode; NBT, 4-nitrobenzenethiol; RE, reference electrode; SAM, self-assembled monolayer; SMU, source measure unit. Panel **a** is reprinted from REF.[65], CC BY 4.0 (https://creativecommons.org/licenses/by/4.0/). Panel **b** reprinted with permission from REF.[296], ACS. Panel **c** reprinted with permission from REF.[263], ACS. Panel **d** reprinted with permission from REF.[332], ACS. Panel **e** is reprinted with permission from REF.[313], Elsevier. Panel **f** reprinted with permission from REF.[21], ACS. Panel **g** reprinted with permission from REF.[241], ACS.

obtain enduring molecular junctions without the need for the chemical modification of molecules anchoring to the electrodes.

Nanoscale light sources in junctions

Plasmonic junctions are able to process illuminating light and electric currents via a shared circuitry unit. In plasmonic nanostructures, LSPs generated by both optical and electrical excitation undergo rapid relaxation via radiative or non-radiative decay, which are interesting in applications involving nanoscale light sources[315,316]. A strong upconversion effect, with generated photon energy ($\hbar\omega$) significantly exceeding the energy threshold of the incident electrons (eV, where V is the applied bias), has been reported in only electrically biased EBJs. The photon yield (emitted photons per incident electrons) is up to $\sim 10^4$ depending on the different electrode materials over two sides[21] (FIG. 9f). With simultaneous optical and electrical excitation in gold–gold EBJs, more than ~1,000-fold upconverted photons are emitted compared with either electrical or optical excitation alone[20]. Moreover, plasmonic nanocavities are known to be highly efficient for non-linear optical absorption and emission[238,317–320]. The light emission can be attributed to the spontaneous emission from a non-equilibrium hot-electron distribution, which arises from the rapidly thermalized tunnelling electrons via inelastic electron–electron scattering. This process is much faster than the coupling to the lattice via electron–phonon scattering[321,322]. For MCBJs, hot-electron gas in electrodes radiating in the infrared range (0.2–1.2 eV) has been reported[323]. The plasmonic structure controls the emission spectrum and polarization, and thus enhances the emission efficiency.

Light emission in point–plane architecture has also been demonstrated for SMJs using different STM approaches[239]. The emitting frequency can be controlled (750–1,000 nm) by carefully selecting the chemical structure of the emitting units in junctions where porphyrin derivatives are suspended from a STM tip and are in contact with a gold surface[241]. Changing the STM tip position to inject charge carriers into different molecular orbitals is another way to tune the wavelength as the excitation of the radiative process with different frequencies can be chosen[324]. The lifetimes of the charged and excited states of the emitting units were controlled by adjusting the thickness of the insulator, which separates the molecule from the lower gold substrate[242]. The photon emission efficiency of the charged molecule has been boosted to 19 times as compared with the neutral states[240]. The enhancement of the emitted photonic intensity is closely related to the electric field across the molecule above a specific threshold (generally, the bias voltage exceeds the optical band gap of the molecule)[221,226–228,243]. Possible light-emitting nanoscale devices based on the concepts of plasmonics are promising because they operate at tunnelling intervals at the scale of femtoseconds. Also, the related response times, limited by the product of resistance (R) and capacitance (C), are short because of their molecular dimension making it possible to operate in a regime greater than terahertz, and the energy to switch a single molecule (and thus the entire devices) is, in principle, low.

Summary and future outlook

This Review has outlined several aspects of plasmonic phenomena in molecular junctions within three typical device architectures, and described the fundamental concepts of plasmon-mediated charge transport phenomena, hot-electron and plasmon–molecule coupling, and potential device applications. However, challenges remain in understanding the underlying mechanisms and achieving functional nanoscale devices. For example, there is still room to improve the conversion efficiency between photons and electrons in molecular junctions. Small variations in metallic electrodes could substantially change their plasmon resonance properties in MCBJs and STM-BJs. At a molecular level, the intrinsic HOMO–LUMO gap of the molecule needs to be considered because it limits the detection bandwidth of molecular junctions.

There are exciting opportunities for linking plasmonics with novel device concepts. First, as molecules with quantum interference effects accommodate two or more electron transport channels, SPPs may modulate the phase of the wavefunction of the channels differently, thereby affecting the quantum interference effect[325,326]. New material interfaces can also be explored with graphene and carbon nanotubes. For instance, graphene-assisted plasmon polaritons can be used in the near infrared, and carbon nanotube excitons, which have excellent electronic properties, can be used to form point contact devices based on carbon instead of metal. The development of highly efficient generation, manipulation and conversion of plasmons in molecular devices would provide additional non-linearity and gain to active molecular emitters, which should enable multiple control methods in all-optical switches[327] and nanolasers[328]. Intense femtosecond and nanosecond-pulsed laser sources can contribute to the investigation of Floquet states and non-linear effects in molecular junctions. Optical trapping and counteracting thermal fields will provide remote and non-invasive approaches in the manipulation of delivery and programmed triggering

of specific biomolecules into target cells under resonant illumination[329]. Finally, tailoring the spectral response of plasmonic resonances with proper modification of the topology of a metal nanostructure and continuous harnessing of a plasmonic-derived hot-electron population are critical to maintain high photostability in high-quality sensing and ever-improving quantum efficiency in sunlight-harvesting technologies.

Improving quantum yields by engineering the barrier heights with either conventional metal–semiconductor junctions or via molecular junctions with versatile transmission characteristics could be the crucial next step to improve the efficiencies of hot carrier-based light to electrical energy harvesting devices to the point where they are of commercial value. In plasmonic redox reactions, the lifetime of transient ions is not well studied, but it likely depends on a large number of factors such as molecular properties, molecule–electrode coupling strength and the shape of the junctions, among others. It is therefore important to study such phenomena in more detail. Fully integrated in vivo biosensors are not ready to be applied in personalized health care. Further improvements in sensitivity, specificity and recognition accuracy in donor–acceptor combination statistics are required. The future application of in vivo biosensors also requires improved device stability and an improved understanding of plasmonic phenomena within molecular junctions. To generate realistic devices for the future, values for operation voltage, switching energies, switching speed and charging and discharging speeds have to be estimated. Furthermore, the full potential of molecular-scale plasmonic–electronic devices is limited by several factors such as the stochastic nature of the quantum mechanical tunnelling phenomena; plasmonic losses in highly confined areas; and the required quantitative consideration of metallic electrodes quenching molecular excited states. Finally, numerous devices exist in which the charge transport through the molecular junctions is incoherent[330]. The mutual impact of plasmonic effects and incoherent charge transport are not very well studied to date and need to be explored further.

Over the past decade, we have witnessed significant progress in investigating and understanding plasmon excitation and out-coupling in the quantum regime, which was previously difficult to access owing to limitations in fabrication methods. With the development of nano fabrication techniques, the research in molecular electronics has highly crossed over with the research of plasmonic optics. On the one hand, plasmonics provides a way to manipulate the electronic transport through molecular junctions with unique nano-focusing characteristics. On the other hand, molecular junctions can influence the plasmonic properties to trigger new applications. By addressing a couple of remaining scientific issues, novel plasmonic molecular devices with high stabilities, satisfying efficiencies and proper multifunctionalities await to emerge in the near future. The answers to the left-open problems will complete the understanding of plasmonic molecular phenomena and principles and will foster novel applications.

Published online 20 September 2022

1. Wehner, M. et al. An integrated design and fabrication strategy for entirely soft, autonomous robots. *Nature* **536**, 451–455 (2016).
2. van de Burgt, Y., Melianas, A., Keene, S. T., Malliaras, G. & Salleo, A. Organic electronics for neuromorphic computing. *Nat. Electron.* **1**, 386–397 (2018).
3. Zhu, J., Zhang, T., Yang, Y. & Huang, R. A comprehensive review on emerging artificial neuromorphic devices. *Appl. Phys. Rev.* **7**, 011312 (2020).
4. Cramer, T. Learning with brain chemistry. *Nat. Mater.* **19**, 934–935 (2020).
5. Goswami, S. et al. Charge disproportionate molecular redox for discrete memristive and memcapacitive switching. *Nat. Nanotech.* **15**, 380–389 (2020).
6. Han, Y. et al. Electric-field-driven dual-functional molecular switches in tunnel junctions. *Nat. Mater.* **19**, 843–848 (2020).
7. Li, T. et al. Integrated molecular diode as 10 MHz half-wave rectifier based on an organic nanostructure heterojunction. *Nat. Commun.* **11**, 3592 (2020).
8. Cuevas, J. C. & Scheer, E. *Molecular Electronics: An Introduction to Theory and Experiment* Vol. 15 (World Scientific, 2017).
This book on molecular electronics covers many fundamental aspects of molecular junctions and their electronic transport behaviour.
9. Aviram, A. & Ratner, M. A. Molecular rectifiers. *Chem. Phys. Lett.* **29**, 277–283 (1974).
10. Thompson, D., Barco, E. D. & Nijhuis, C. A. Design principles of dual-functional molecular switches in solid-state tunnel junctions. *Appl. Phys. Lett.* **117**, 030502 (2020).
11. Su, T. A., Neupane, M., Steigerwald, M. L., Venkataraman, L. & Nuckolls, C. Chemical principles of single-molecule electronics. *Nat. Rev. Mater.* **1**, 16002 (2016).
This work is a seminal review on structure–property relationships of the electrodes, anchoring groups and molecular bridge in a SMJ.
12. Jeong, H., Kim, D., Xiang, D. & Lee, T. High-yield functional molecular electronic devices. *ACS Nano* **11**, 6511–6548 (2017).
13. Xiang, D., Wang, X., Jia, C., Lee, T. & Guo, X. Molecular-scale electronics: from concept to function. *Chem. Rev.* **116**, 4318–4440 (2016).
This work is a comprehensive review covering the major concepts and applications in molecular electronics.
14. Gehring, P., Thijssen, J. M. & van der Zant, H. S. J. Single-molecule quantum-transport phenomena in break junctions. *Nat. Rev. Phys.* **1**, 381–396 (2019).
This work is a seminal review on quantum features characterized by various energy scales in break junctions.
15. Xu, B. & Tao, N. J. Measurement of single-molecule resistance by repeated formation of molecular junctions. *Science* **301**, 1221–1223 (2003).
16. Venkataraman, L., Klare, J. E., Nuckolls, C., Hybertsen, M. S. & Steigerwald, M. L. Dependence of single-molecule junction conductance on molecular conformation. *Nature* **442**, 904–907 (2006).
17. Reed, M. A., Zhou, C., Muller, C. J., Burgin, T. P. & Tour, J. M. Conductance of a molecular junction. *Science* **278**, 252 (1997).
18. Wang, L., Wang, L., Zhang, L. & Xiang, D. Advance of mechanically controllable break junction for molecular electronics. *Top. Curr. Chem.* **375**, 61 (2017).
19. Park, H., Lim, A. K. L., Alivisatos, A. P., Park, J. & McEuen, P. L. Fabrication of metallic electrodes with nanometer separation by electromigration. *Appl. Phys. Lett.* **75**, 301–303 (1999).
20. Cui, L., Zhu, Y., Nordlander, P., Di Ventra, M. & Natelson, D. Thousand-fold increase in plasmonic light emission via combined electronic and optical excitations. *Nano Lett.* **21**, 2658–2665 (2021).
21. Cui, L. et al. Electrically driven hot-carrier generation and above-threshold light emission in plasmonic tunnel junctions. *Nano Lett.* **20**, 6067–6075 (2020).
22. Xu, B., Xiao, X. & Tao, N. J. Measurements of single-molecule electromechanical properties. *J. Am. Chem. Soc.* **125**, 16164–16165 (2003).
23. Baumberg, J. J., Aizpurua, J., Mikkelsen, M. H. & Smith, D. R. Extreme nanophotonics from ultrathin metallic gaps. *Nat. Mater.* **18**, 668–678 (2019).
This work is a recent review on the plasmonic properties of NPoMJs.
24. Li, G.-C., Zhang, Q., Maier, S. A. & Lei, D. Plasmonic particle-on-film nanocavities: a versatile platform for plasmon-enhanced spectroscopy and photochemistry. *Nanophotonics* **7**, 1865–1889 (2018).
25. Akkerman, H. B., Blom, P. W., de Leeuw, D. M. & de Boer, B. Towards molecular electronics with large-area molecular junctions. *Nature* **441**, 69–72 (2006).
26. Vilan, A., Aswal, D. & Cahen, D. Large-area, ensemble molecular electronics: motivation and challenges. *Chem. Rev.* **117**, 4248–4286 (2017).
27. Morteza Najarian, A., Szeto, B., Tefashe, U. M. & McCreery, R. L. Robust all-carbon molecular junctions on flexible or semi-transparent substrates using "process-friendly" fabrication. *ACS Nano* **10**, 8918–8928 (2016).
28. Najarian, A. M., Supur, M. & McCreery, R. L. Electrostatic redox reactions and charge storage in molecular electronic junctions. *J. Phys. Chem. C.* **124**, 1739–1748 (2020).
29. Lacroix, J. C. Electrochemistry does the impossible: robust and reliable large area molecular junctions. *Curr. Opin. Electrochem.* **7**, 153–160 (2018).
30. Jiang, N., Zhuo, X. & Wang, J. Active plasmonics: principles, structures, and applications. *Chem. Rev.* **118**, 3054–3099 (2018).
31. Amendola, V., Pilot, R., Frasconi, M., Maragò, O. M. & Iatì, M. A. Surface plasmon resonance in gold nanoparticles: a review. *J. Phys. Condens. Matter* **29**, 203002 (2017).
32. Minamimoto, H., Oikawa, S., Li, X. & Murakoshi, K. Plasmonic fields focused to molecular size. *ChemNanoMat* **3**, 843–856 (2017).
33. Kildishev, A. V., Boltasseva, A. & Shalaev, V. M. Planar photonics with metasurfaces. *Science* **339**, 1232009 (2013).
34. Yang, A., Wang, D., Wang, W. & Odom, T. W. Coherent light sources at the nanoscale. *Annu. Rev. Phys. Chem.* **68**, 83–99 (2017).

35. Li, J. et al. Plasmon-induced resonance energy transfer for solar energy conversion. *Nat. Photon.* **9**, 601–607 (2015).
36. Roelli, P., Galland, C., Piro, N. & Kippenberg, T. J. Molecular cavity optomechanics as a theory of plasmon-enhanced Raman scattering. *Nat. Nanotech.* **11**, 164–169 (2016).
37. Zhu, W. et al. Quantum mechanical effects in plasmonic structures with subnanometre gaps. *Nat. Commun.* **7**, 11495 (2016).
This work is a seminal review on critical quantum effects in plasmonic nanogaps.
38. Arielly, R., Ofarim, A., Noy, G. & Selzer, Y. Accurate determination of plasmonic fields in molecular junctions by current rectification at optical frequencies. *Nano Lett.* **11**, 2968–2972 (2011).
39. Duffin, T. J. et al. Cavity plasmonics in tunnel junctions: outcoupling and the role of surface roughness. *Phys. Rev. Appl.* **14**, 044021 (2020).
40. Makarenko, K. S. et al. Efficient surface plasmon polariton excitation and control over outcoupling mechanisms in metal–insulator–metal tunneling junctions. *Adv. Sci.* **7**, 1900291 (2020).
41. Lin, L. et al. Nanooptics of plasmonic nanomatryoshkas: shrinking the size of a core–shell junction to subnanometer. *Nano Lett.* **15**, 6419–6428 (2015).
42. Aguirregabiria, G. et al. Role of electron tunneling in the nonlinear response of plasmonic nanogaps. *Phys. Rev. B* **97**, 115430 (2018).
43. Chikkaraddy, R. et al. Single-molecule strong coupling at room temperature in plasmonic nanocavities. *Nature* **535**, 127–130 (2016).
This article reports the achievement of strong coupling in single-emitter devices at ambient conditions.
44. Tan, S. F. et al. Quantum plasmon resonances controlled by molecular tunnel junctions. *Science* **343**, 1496–1499 (2014).
This seminal paper demonstrates CTP modes in silver nanocube dimers.
45. Barbry, M. et al. Atomistic near-field nanoplasmonics: reaching atomic-scale resolution in nanooptics. *Nano Lett.* **15**, 3410–3419 (2015).
46. Esteban, R. et al. A classical treatment of optical tunneling in plasmonic gaps: extending the quantum corrected model to practical situations. *Faraday Discuss.* **178**, 151–183 (2015).
47. Wang, T. & Nijhuis, C. A. Molecular electronic plasmonics. *Appl. Mater. Today* **3**, 73–86 (2016).
48. Pal, P. P. et al. Plasmon-mediated electron transport in tip-enhanced Raman spectroscopic junctions. *J. Phys. Chem. Lett.* **6**, 4210–4218 (2015).
49. Klimov, V. V. & Guzatov, D. V. Plasmonic atoms and plasmonic molecules. *Appl. Phys. A* **89**, 305–314 (2007).
50. Kim, Y. Photoswitching molecular junctions: platforms and electrical properties. *ChemPhysChem* **21**, 2368–2383 (2020).
51. Galperin, M. & Nitzan, A. Molecular optoelectronics: the interaction of molecular conduction junctions with light. *Phys. Chem. Chem. Phys.* **14**, 9421–9438 (2012).
52. Langer, J. et al. Present and future of surface-enhanced Raman scattering. *ACS Nano* **14**, 28–117 (2020).
53. Lee, J., Jeon, D.-J. & Yeo, J.-S. Quantum plasmonics: energy transport through plasmonic gap. *Adv. Mater.* **33**, e2006606 (2021).
This work is a comprehensive review of the latest developments in quantum plasmonic resonators.
54. Sivan, Y., Un, I. W. & Dubi, Y. Assistance of metal nanoparticles in photocatalysis — nothing more than a classical heat source. *Faraday Discuss.* **214**, 215–233 (2019).
55. Furube, A. & Hashimoto, S. Insight into plasmonic hot-electron transfer and plasmon molecular drive: new dimensions in energy conversion and nanofabrication. *NPG Asia Mater.* **9**, e454 (2017).
56. Wang, J. et al. Photothermal reshaping of gold nanoparticles in a plasmonic absorber. *Opt. Express* **19**, 14726–14734 (2011).
57. Nitzan, A. Electron transmission through molecules and molecular interfaces. *Annu. Rev. Phys. Chem.* **52**, 681–750 (2001).
58. Fung, E. D., Adak, O., Lovat, G., Scarabelli, D. & Venkataraman, L. Too hot for photon-assisted transport: hot-electrons dominate conductance enhancement in illuminated single-molecule junctions. *Nano Lett.* **17**, 1255–1261 (2017).
59. Jauho, A.-P., Wingreen, N. S. & Meir, Y. Time-dependent transport in interacting and noninteracting resonant-tunneling systems. *Phys. Rev. B* **50**, 5528–5544 (1994).
60. Tien, P. K. & Gordon, J. P. Multiphoton process observed in the interaction of microwave fields with the tunneling between superconductor films. *Phys. Rev.* **129**, 647–651 (1963).
61. Tucker, J. Quantum limited detection in tunnel junction mixers. *IEEE J. Quantum Electron.* **15**, 1234–1258 (1979).
62. Ward, D. R., Hüser, F., Pauly, F., Cuevas, J. C. & Natelson, D. Optical rectification and field enhancement in a plasmonic nanogap. *Nat. Nanotech* **5**, 732–736 (2010).
This seminal paper discusses the physical origin of optical rectification in nanogaps.
63. Noy, G., Ophir, A. & Selzer, Y. Response of molecular junctions to surface plasmon polaritons. *Angew. Chem. Int. Ed.* **49**, 5734–5736 (2010).
64. Vadai, M. et al. Plasmon-induced conductance enhancement in single-molecule junctions. *J. Phys. Chem. Lett.* **4**, 2811–2816 (2013).
65. Kos, D., Assumpcao, D. R., Guo, C. & Baumberg, J. J. Quantum tunneling induced optical rectification and plasmon-enhanced photocurrent in nanocavity molecular junctions. *ACS Nano* **15**, 14535–14543 (2021).
66. McFarland, E. W. & Tang, J. A photovoltaic device structure based on internal electron emission. *Nature* **421**, 616–618 (2003).
67. Dubi, Y. & Sivan, Y. "Hot" electrons in metallic nanostructures — non-thermal carriers or heating? *Light Sci. Appl.* **8**, 89 (2019).
This work presents a mechanistic discrimination of hot electrons and thermal effects in plasmonic nanostructures.
68. Guo, Q., Ma, Z., Zhou, C., Ren, Z. & Yang, X. Single molecule photocatalysis on TiO_2 surfaces. *Chem. Rev.* **119**, 11020–11041 (2019).
69. Mahapatra, S., Schultz, J. F., Li, L., Zhang, X. & Jiang, N. Controlling localized plasmons via an atomistic approach: attainment of site-selective activation inside a single molecule. *J. Am. Chem. Soc.* **144**, 2051–2055 (2022).
70. Nguyen, V.-Q., Ai, Y., Martin, P. & Lacroix, J.-C. Plasmon-induced nanolocalized reduction of diazonium salts. *ACS Omega* **2**, 1947–1955 (2017).
71. Galperin, M., Nitzan, A. & Ratner, M. A. Molecular transport junctions: current from electronic excitations in the leads. *Phys. Rev. Lett.* **96**, 166803 (2006).
72. Jou, D., Sellitto, A. & Cimmelli, V. A. Phonon temperature and electron temperature in thermoelectric coupling. *J. Non-Equilib. Thermodyn.* **38**, 335–361 (2013).
73. Pothier, H., Guéron, S., Birge, N. O., Esteve, D. & Devoret, M. H. Energy distribution function of quasiparticles in mesoscopic wires. *Phys. Rev. Lett.* **79**, 3490–3493 (1997).
74. Clavero, C. Plasmon-induced hot-electron generation at nanoparticle/metal-oxide interfaces for photovoltaic and photocatalytic devices. *Nat. Photon.* **8**, 95–103 (2014).
75. Cvetko, D. et al. Ultrafast electron injection into photo-excited organic molecules. *Phys. Chem. Chem. Phys.* **18**, 22140–22145 (2016).
76. Yoshida, K., Shibata, K. & Hirakawa, K. Terahertz field enhancement and photon-assisted tunneling in single-molecule transistors. *Phys. Rev. Lett.* **115**, 138302 (2015).
77. Cocker, T. L., Peller, D., Yu, P., Repp, J. & Huber, R. Tracking the ultrafast motion of a single molecule by femtosecond orbital imaging. *Nature* **539**, 263–267 (2016).
78. Washburn, S. & Webb, R. A. Aharonov–Bohm effect in normal metal quantum coherence and transport. *Adv. Phys.* **35**, 375–422 (1986).
79. Hattori, Y. et al. Phonon-assisted hot carrier generation in plasmonic semiconductor systems. *Nano Lett.* **21**, 1083–1089 (2021).
80. Sivan, Y. & Dubi, Y. Recent developments in plasmon-assisted photocatalysis — a personal perspective. *Appl. Phys. Lett.* **117**, 130501 (2020).
81. Sivan, Y., Baraban, J., Un, I. W. & Dubi, Y. Comment on "Quantifying hot carrier and thermal contributions in plasmonic photocatalysis". *Science* **364**, eaaw9367 (2019).
82. Wang, J., Wang, X. & Mu, X. Plasmonic photocatalysts monitored by tip-enhanced Raman spectroscopy. *Catalysts* **9**, 109 (2019).
83. Kazuma, E., Jung, J., Ueba, H., Trenary, M. & Kim, Y. Real-space and real-time observation of a plasmon-induced chemical reaction of a single molecule. *Science* **360**, 521–525 (2018).
This study monitors a direct intramolecular plasmonic excitation to trigger a chemical reaction.
84. Boerigter, C., Aslam, U. & Linic, S. Mechanism of charge transfer from plasmonic nanostructures to chemically attached materials. *ACS Nano* **10**, 6108–6115 (2016).
85. Olson, J. et al. Optical characterization of single plasmonic nanoparticles. *Chem. Soc. Rev.* **44**, 40–57 (2015).
86. Foerster, B. et al. Chemical interface damping depends on electrons reaching the surface. *ACS Nano* **11**, 2886–2893 (2017).
87. Hoggard, A. et al. Using the plasmon linewidth to calculate the time and efficiency of electron transfer between gold nanorods and graphene. *ACS Nano* **7**, 11209–11217 (2013).
88. Juvé, V. et al. Size-dependent surface plasmon resonance broadening in nonspherical nanoparticles: single gold nanorods. *Nano Lett.* **13**, 2234–2240 (2013).
89. Kazuma, E., Lee, M., Jung, J., Trenary, M. & Kim, Y. Single-molecule study of a plasmon-induced reaction for a strongly chemisorbed molecule. *Angew. Chem. Int. Ed.* **59**, 7960–7966 (2020).
90. Linic, S., Christopher, P. & Ingram, D. B. Plasmonic–metal nanostructures for efficient conversion of solar to chemical energy. *Nat. Mater.* **10**, 911–921 (2011).
91. Xiang, B., Li, Y., Pham, C. H., Paesani, F. & Xiong, W. Ultrafast direct electron transfer at organic semiconductor and metal interfaces. *Sci. Adv.* **3**, e1701508 (2017).
92. Ayzner, A. L., Nordlund, D., Kim, D.-H., Bao, Z. & Toney, M. F. Ultrafast electron transfer at organic semiconductor interfaces: importance of molecular orientation. *J. Phys. Chem. Lett.* **6**, 6–12 (2015).
93. Zhang, W. et al. Atomic switches of metallic point contacts by plasmonic heating. *Light. Sci. Appl.* **8**, 34 (2019).
This work presents a direct observation of conductance switching owing to thermal expansion of metallic electrodes.
94. Grafström, S., Schuller, P., Kowalski, J. & Neumann, R. Thermal expansion of scanning tunneling microscopy tips under laser illumination. *J. Appl. Phys.* **83**, 3453–3460 (1998).
95. Boneberg, J., Tresp, M., Ochmann, M., Münzer, H. J. & Leiderer, P. Time-resolved measurements of the response of a STM tip upon illumination with a nanosecond laser pulse. *Appl. Phys. A* **66**, 615–619 (1998).
96. Boneberg, J., Münzer, H. J., Tresp, M., Ochmann, M. & Leiderer, P. The mechanism of nanostructuring upon nanosecond laser irradiation of a STM tip. *Appl. Phys. A.* **67**, 381–384 (1998).
97. Benner, D. et al. Transmission of surface plasmon polaritons through atomic-size constrictions. *New J. Phys.* **15**, 113014 (2013).
98. Benner, D. et al. Lateral and temporal dependence of the transport through an atomic gold contact under light irradiation: signature of propagating surface plasmon polaritons. *Nano Lett.* **14**, 5218–5223 (2014).
99. Zhang, S. et al. In-situ control of on-chip angstrom gaps, atomic switches, and molecular junctions by light irradiation. *Nano Today* **39**, 101226 (2021).
100. Cui, L. et al. Thermal conductance of single-molecule junctions. *Nature* **572**, 628–633 (2019).
This seminal paper determines thermal electronic transport by STM-BJs.
101. Wang, K., Meyhofer, E. & Reddy, P. Thermal and thermoelectric properties of molecular junctions. *Adv. Funct. Mater.* **30**, 1904534 (2020).
102. Scheinert, S. et al. Contact characterization by photoemission and device performance in P3HT based organic transistors. *J. Appl. Phys.* **111**, 064502 (2012).
103. Forati, E., Dill, T. J., Tao, A. R. & Sievenpiper, D. Photoemission-based microelectronic devices. *Nat. Commun.* **7**, 13399 (2016).
104. Lambe, J. & McCarthy, S. L. Light emission from inelastic electron tunneling. *Phys. Rev. Lett.* **37**, 923–925 (1976).
105. Zhou, J., Wang, K., Xu, B. & Dubi, Y. Photoconductance from exciton binding in molecular junctions. *J. Am. Chem. Soc.* **140**, 70–73 (2018).
106. Perrin, M. L. et al. Large tunable image-charge effects in single-molecule junctions. *Nat. Nanotech.* **8**, 282–287 (2013).
107. Cortese, E. et al. Excitons bound by photon exchange. *Nat. Phys.* **17**, 31–35 (2021).
108. Bjork, G., Machida, S., Yamamoto, Y. & Igeta, K. Modification of spontaneous emission rate in planar dielectric microcavity structures. *Phys. Rev. A* **44**, 669–681 (1991).
109. Petoukhoff, C. E., Dani, K. M. & O'Carroll, D. M. Strong plasmon-exciton coupling in Ag nanoparticle-conjugated polymer core–shell hybrid nanostructures. *Polymers* **12**, 2141 (2020).

110. Pompa, P. P. et al. Metal-enhanced fluorescence of colloidal nanocrystals with nanoscale control. *Nat. Nanotech.* **1**, 126–130 (2006).
111. Kitajima, Y., Sakamoto, H. & Ueno, K. Coupled plasmonic systems: controlling the plasmon dynamics and spectral modulations for molecular detection. *Nanoscale* **13**, 5187–5201 (2021).
112. Chen, H. et al. Plasmon–molecule interactions. *Nano Today* **5**, 494–505 (2010).
113. Rossi, T. P., Shegai, T., Erhart, P. & Antosiewicz, T. J. Strong plasmon–molecule coupling at the nanoscale revealed by first-principles modeling. *Nat. Commun.* **10**, 3336 (2019).
114. Liu, W. et al. Understanding the different exciton–plasmon coupling regimes in two-dimensional semiconductors coupled with plasmonic lattices: a combined experimental and unified equation of motion approach. *ACS Photonics* **5**, 192–204 (2018).
115. Hugall, J. T., Singh, A. & van Hulst, N. F. Plasmonic cavity coupling. *ACS Photonics* **5**, 43–53 (2018).
116. Russell, K. J., Yeung, K. Y. M. & Hu, E. Measuring the mode volume of plasmonic nanocavities using coupled optical emitters. *Phys. Rev. B* **85**, 245445 (2012).
117. Martín-Jiménez, A. et al. Unveiling the radiative local density of optical states of a plasmonic nanocavity by STM. *Nat. Commun.* **11**, 1021 (2020).
118. Cuartero-González, A. & Fernández-Domínguez, A. I. Dipolar and quadrupolar excitons coupled to a nanoparticle-on-mirror cavity. *Phys. Rev. B* **101**, 035403 (2020).
119. Li, Y. et al. Time-resolved photoluminescence spectroscopy of exciton–plasmon coupling dynamics. *Plasmonics* **10**, 271–280 (2015).
120. Zengin, G. et al. Evaluating conditions for strong coupling between nanoparticle plasmons and organic dyes using scattering and absorption spectroscopy. *J. Phys. Chem. C* **120**, 20588–20596 (2016).
121. Zhang, P., Jin, W. & Liang, W. Size-dependent optical properties of aluminum nanoparticles: from classical to quantum description. *J. Phys. Chem. C* **122**, 10545–10551 (2018).
122. Kang, E. S. H. et al. Strong plasmon–exciton coupling with directional absorption features in optically thin hybrid nanohole metasurfaces. *ACS Photonics* **5**, 4046–4055 (2018).
123. Shahbazyan, T. V. Transition to strong coupling regime in hybrid plasmonic systems: exciton-induced transparency and Fano interference. *Nanophotonics* **10**, 20210246 (2021).
124. Ridolfo, A., Di Stefano, O., Fina, N., Saija, R. & Savasta, S. Quantum plasmonics with quantum dot–metal nanoparticle molecules: influence of the Fano effect on photon statistics. *Phys. Rev. Lett.* **105**, 263601 (2010).
125. Cacciola, A., Di Stefano, O., Stassi, R., Saija, R. & Savasta, S. Ultrastrong coupling of plasmons and excitons in a nanoshell. *ACS Nano* **8**, 11483–11492 (2014).
126. Pelton, M., Storm, S. D. & Leng, H. Strong coupling of emitters to single plasmonic nanoparticles: exciton-induced transparency and Rabi splitting. *Nanoscale* **11**, 14540–14552 (2019).
127. Zengin, G. et al. Approaching the strong coupling limit in single plasmonic nanorods interacting with J-aggregates. *Sci. Rep.* **3**, 3074 (2013).
128. Barnes, W. L., Horsley, S. A. R. & Vos, W. L. Classical antennae, quantum emitters, and densities of optical states. *J. Opt*. https://doi.org/10.1088/2040-8986/ab7b01 (2020).
129. Pelton, M. Modified spontaneous emission in nanophotonic structures. *Nat. Photon.* **9**, 427–435 (2015).
130. Bergfield, J. P. & Hendrickson, J. R. Signatures of plexcitonic states in molecular electroluminescence. *Sci. Rep.* **8**, 2314 (2018).
131. Lu, X., Ye, G., Punj, D., Chiechi, R. C. & Orrit, M. Quantum yield limits for the detection of single-molecule fluorescence enhancement by a gold nanorod. *ACS Photonics* **7**, 2498–2505 (2020).
132. Grynberg, G., Aspect, A. & Fabre, C. *Introduction to Quantum Optics: From the Semi-classical Approach to Quantized Light* (Cambridge Univ. Press, 2010).
133. Javanainen, J. Quantum optics: an introduction. *Phys. Today* **60**, 74–75 (2007).
134. Haran, G. & Chuntonov, L. Artificial plasmonic molecules and their interaction with real molecules. *Chem. Rev.* **118**, 5539–5580 (2018).
135. Vilan, A. & Cahen, D. Chemical modification of semiconductor surfaces for molecular electronics. *Chem. Rev.* **117**, 4624–4666 (2017).
136. Park, J.-E., Kim, J. & Nam, J.-M. Emerging plasmonic nanostructures for controlling and enhancing photoluminescence. *Chem. Sci.* **8**, 4696–4704 (2017).
137. Linic, S., Chavez, S. & Elias, R. Flow and extraction of energy and charge carriers in hybrid plasmonic nanostructures. *Nat. Mater.* **20**, 916–924 (2021).
138. Cunha, J. et al. Controlling light, heat, and vibrations in plasmonics and phononics. *Adv. Opt. Mater.* **8**, 2001225 (2020).
139. Aradhya, S. V., Frei, M., Hybertsen, M. S. & Venkataraman, L. Van der Waals interactions at metal/organic interfaces at the single-molecule level. *Nat. Mater.* **11**, 872–876 (2012).
This seminal paper discusses structure properties at the interface of metal electrodes and molecules.
140. Pérez-González, O. et al. Optical spectroscopy of conductive junctions in plasmonic cavities. *Nano Lett.* **10**, 3090–3095 (2010).
141. Křápek, V. et al. Independent engineering of individual plasmon modes in plasmonic dimers with conductive and capacitive coupling. *Nanophotonics* **9**, 623–632 (2020).
142. Wu, L. et al. Charge transfer plasmon resonances across silver–molecule–silver junctions: estimating the terahertz conductance of molecules at near-infrared frequencies. *RSC Adv.* **6**, 70884–70894 (2016).
143. Gurlek, B., Sandoghdar, V. & Martín-Cano, D. Manipulation of quenching in nanoantenna–emitter systems enabled by external detuned cavities: a path to enhance strong-coupling. *ACS Photonics* **5**, 456–461 (2018).
144. Amin, R. et al. Active material, optical mode and cavity impact on nanoscale electro-optic modulation performance. *Nanophotonics* **7**, 455–472 (2018).
145. Vora, P. M. et al. Spin–cavity interactions between a quantum dot molecule and a photonic crystal cavity. *Nat. Commun.* **6**, 7665 (2015).
146. Mokkath, J. H. & Henzie, J. An asymmetric aluminum active quantum plasmonic device. *Phys. Chem. Chem. Phys.* **22**, 1416–1421 (2020).
147. Shibata, K., Fujii, S., Sun, Q., Miura, A. & Ueno, K. Further enhancement of the near-field on Au nanogap dimers using quasi-dark plasmon modes. *J. Chem. Phys.* **152**, 104706 (2020).
148. Esteban, R., Borisov, A. G., Nordlander, P. & Aizpurua, J. Bridging quantum and classical plasmonics with a quantum-corrected model. *Nat. Commun.* **3**, 825 (2012).
149. Brown, L. V., Sobhani, H., Lassiter, J. B., Nordlander, P. & Halas, N. J. Heterodimers: plasmonic properties of mismatched nanoparticle pairs. *ACS Nano* **4**, 819–832 (2010).
150. Jeong, H.-H. et al. Arrays of plasmonic nanoparticle dimers with defined nanogap spacers. *ACS Nano* **13**, 11453–11459 (2019).
151. Zohar, N., Chuntonov, L. & Haran, G. The simplest plasmonic molecules: metal nanoparticle dimers and trimers. *J. Photochem. Photobiol. C. Photochem. Rev.* **21**, 26–39 (2014).
152. Jain, P. K., Huang, W. & El-Sayed, M. A. On the universal scaling behavior of the distance decay of plasmon coupling in metal nanoparticle pairs: a plasmon ruler equation. *Nano Lett.* **7**, 2080–2088 (2007).
153. Wang, T. et al. Phonon–polaritonic bowtie nanoantennas: controlling infrared thermal radiation at the nanoscale. *ACS Photonics* **4**, 1753–1760 (2017).
154. Tsai, C.-Y. et al. Plasmonic coupling in gold nanoring dimers: observation of coupled bonding mode. *Nano Lett.* **12**, 1648–1654 (2012).
155. Alkan, F. & Aikens, C. M. Understanding plasmon coupling in nanoparticle dimers using molecular orbitals and configuration interaction. *Phys. Chem. Chem. Phys.* **21**, 23065–23075 (2019).
156. Merlein, J. et al. Nanomechanical control of an optical antenna. *Nat. Photon.* **2**, 230–233 (2008).
157. Marinica, D. C., Kazansky, A. K., Nordlander, P., Aizpurua, J. & Borisov, A. G. Quantum plasmonics: nonlinear effects in the field enhancement of a plasmonic nanoparticle dimer. *Nano Lett.* **12**, 1333–1339 (2012).
158. Nordlander, P., Oubre, C., Prodan, E., Li, K. & Stockman, M. I. Plasmon hybridization in nanoparticle dimers. *Nano Lett.* **4**, 899–903 (2004).
159. Zhang, Q. et al. Electron energy-loss spectroscopy of spatial nonlocality and quantum tunneling effects in the bright and dark plasmon modes of gold nanosphere dimers. *Adv. Quantum Technol.* **1**, 1800016 (2018).
160. Yu, H. et al. Near-field spectral properties of coupled plasmonic nanoparticle arrays. *Opt. Express* **25**, 6883–6894 (2017).
161. Scholl, J. A., García-Etxarri, A., Koh, A. L. & Dionne, J. A. Observation of quantum tunneling between two plasmonic nanoparticles. *Nano Lett.* **13**, 564–569 (2013).
162. Savage, K. J. et al. Revealing the quantum regime in tunnelling plasmonics. *Nature* **491**, 574–577 (2012).
This article reports direct experimental observation of CTP modes in point–point junctions.
163. Huang, Y., Zhou, Q., Hou, M., Ma, L. & Zhang, Z. Nanogap effects on near- and far-field plasmonic behaviors of metallic nanoparticle dimers. *Phys. Chem. Chem. Phys.* **17**, 29293–29298 (2015).
164. Haq, S., Tesema, T. E., Patra, B., Gomez, E. & Habteyes, T. G. Tuning plasmonic coupling from capacitive to conductive regimes via atomic control of dielectric spacing. *ACS Photonics* **7**, 622–629 (2020).
165. Liu, P., Chulhai, D. V. & Jensen, L. Atomistic characterization of plasmonic dimers in the quantum size regime. *J. Phys. Chem. C* **123**, 13900–13907 (2019).
166. Sun, G., Khurgin, J. B. & Bratkovsky, A. Coupled-mode theory of field enhancement in complex metal nanostructures. *Phys. Rev. B* **84**, 045415 (2011).
167. Braun, K. et al. Active optical antennas driven by inelastic electron tunneling. *Nanophotonics* **7**, 1503–1516 (2018).
168. Sun, G. & Khurgin, J. B. Comparative study of field enhancement between isolated and coupled metal nanoparticles: an analytical approach. *Appl. Phys. Lett.* **97**, 263110 (2010).
169. Ahn, J. S. et al. Optical field enhancement of nanometer-sized gaps at near-infrared frequencies. *Opt. Express* **23**, 4897–4907 (2015).
170. Chen, W. et al. Probing the limits of plasmonic enhancement using a two-dimensional atomic crystal probe. *Light Sci. Appl.* **7**, 56 (2018).
171. Yu, Y. et al. Roadmap for single-molecule surface-enhanced Raman spectroscopy. *Adv. Photonics* **2**, 014002 (2020).
172. Kiguchi, M., Aiba, A., Fujii, S. & Kobayashi, S. Surface enhanced Raman scattering on molecule junction. *Appl. Mater. Today* **14**, 76–83 (2019).
173. Zhan, C. et al. From plasmon-enhanced molecular spectroscopy to plasmon-mediated chemical reactions. *Nat. Rev. Chem.* **2**, 216–230 (2018).
174. Ding, S.-Y. et al. Nanostructure-based plasmon-enhanced Raman spectroscopy for surface analysis of materials. *Nat. Rev. Mater.* **1**, 16021 (2016).
175. Liu, N. & Liedl, T. DNA-assembled advanced plasmonic architectures. *Chem. Rev.* **118**, 3032–3053 (2018).
176. Xu, L., Sun, M., Ma, W., Kuang, H. & Xu, C. Self-assembled nanoparticle dimers with contemporarily relevant properties and emerging applications. *Mater. Today* **19**, 595–606 (2016).
177. Thilagam, R. & Gnanamani, A. Preparation, characterization and stability assessment of keratin and albumin functionalized gold nanoparticles for biomedical applications. *Appl. Nanosci.* **10**, 1879–1892 (2020).
178. Dumur, F., Dumas, E. & Mayer, C. R. Functionalization of gold nanoparticles by inorganic entities. *Nanomaterials* **10**, 548 (2020).
179. Spampinato, V., Parracino, M. A., La Spina, R., Rossi, F. & Ceccone, G. Surface analysis of gold nanoparticles functionalized with thiol-modified glucose SAMs for biosensor applications. *Front. Chem.* **4**, 8 (2016).
180. Lin, L. et al. Electron transport across plasmonic molecular nanogaps interrogated with surface-enhanced Raman scattering. *ACS Nano* **12**, 6492–6503 (2018).
181. Koya, A. N. & Lin, J. Charge transfer plasmons: recent theoretical and experimental developments. *Appl. Phys. Rev.* **4**, 021104 (2017).
182. Lerch, S. & Reinhard, B. M. Effect of interstitial palladium on plasmon-driven charge transfer in nanoparticle dimers. *Nat. Commun.* **9**, 1608 (2018).
183. Iwane, M., Fujii, S. & Kiguchi, M. Surface-enhanced Raman scattering in molecular junctions. *Sensors* **17**, 1901 (2017).
184. Banerjee, P. et al. Plasmon-induced electrical conduction in molecular devices. *ACS Nano* **4**, 1019–1025 (2010).
185. Benz, F. et al. Nanooptics of molecular-shunted plasmonic nanojunctions. *Nano Lett.* **15**, 669–674 (2015).
186. Kadkhodazadeh, S. et al. Scaling of the surface plasmon resonance in gold and silver dimers probed by EELS. *J. Phys. Chem. C* **118**, 5478–5485 (2014).
187. Koh, A. L., Fernández-Domínguez, A. I., McComb, D. W., Maier, S. A. & Yang, J. K. W. High-resolution mapping of electron-beam-excited plasmon modes in lithographically defined gold nanostructures. *Nano Lett.* **11**, 1323–1330 (2011).
188. Scholl, J. A., Koh, A. L. & Dionne, J. A. Quantum plasmon resonances of individual metallic nanoparticles. *Nature* **483**, 421–427 (2012).

189. Raman, K., Konyar, M. & Çetin, E. in *2018 IEEE 13th Nanotechnology Materials and Devices Conference (NMDC)* 1–4 (IEEE, 2018).
190. Zhao, Z. et al. In situ photoconductivity measurements of imidazole in optical fiber break-junctions. *Nanoscale Horiz.* **6**, 386–392 (2021).
191. Song, H. et al. Observation of molecular orbital gating. *Nature* **462**, 1039–1043 (2009).
192. Martin, C. A., van Ruitenbeek, J. M. & van der Zant, H. S. J. Sandwich-type gated mechanical break junctions. *Nanotechnology* **21**, 265201 (2010).
193. Xiang, D. et al. Three-terminal single-molecule junctions formed by mechanically controllable break junctions with side gating. *Nano Lett.* **13**, 2809–2813 (2013).
194. Gruber, C. M. et al. Resonant optical antennas with atomic-sized tips and tunable gaps achieved by mechanical actuation and electrical control. *Nano Lett.* **20**, 4346–4353 (2020).
195. Guo, C. et al. Molecular orbital gating surface-enhanced Raman scattering. *ACS Nano* **12**, 11229–11235 (2018).
196. Zhao, Z. et al. Molecular devices: shaping the atomic-scale geometries of electrodes to control optical and electrical performance of molecular devices (Small 15/2018). *Small* **14**, 1870066 (2018).
197. Laible, F. et al. A flexible platform for controlled optical and electrical effects in tailored plasmonic break junctions. *Nanophotonics* **9**, 1391 (2020).
198. Li, Z. & Xu, H. Nanoantenna effect of surface-enhanced Raman scattering: managing light with plasmons at the nanometer scale. *Adv. Phys. X* **1**, 492–521 (2016).
199. Dao, T. D. et al. Dark-field scattering and local SERS mapping from plasmonic aluminum bowtie antenna array. *Micromachines* **10**, 468 (2019).
200. Baik, J. M., Lee, S. J. & Moskovits, M. Polarized surface-enhanced Raman spectroscopy from molecules adsorbed in nano-gaps produced by electromigration in silver nanowires. *Nano Lett.* **9**, 672–676 (2009).
201. Mubeen, S. et al. Plasmonic properties of gold nanoparticles separated from a gold mirror by an ultrathin oxide. *Nano Lett.* **12**, 2088–2094 (2012).
202. Wei, H. & Xu, H. Hot spots in different metal nanostructures for plasmon-enhanced Raman spectroscopy. *Nanoscale* **5**, 10794–10805 (2013).
203. Zhang, S. & Xu, H. Tunable dark plasmons in a metallic nanocube dimer: toward ultimate sensitivity nanoplasmonic sensors. *Nanoscale* **8**, 13722–13729 (2016).
204. Gao, Y., Zhou, N., Shi, Z., Guo, X. & Tong, L. Dark dimer mode excitation and strong coupling with a nanorod dipole. *Photonics Res.* **6**, 887–892 (2018).
205. Herzog, J. B. et al. Dark plasmons in hot spot generation and polarization in interelectrode nanoscale junctions. *Nano Lett.* **13**, 1359–1364 (2013).
206. Zolotavin, P., Evans, C. & Natelson, D. Photothermoelectric effects and large photovoltages in plasmonic Au nanowires with nanogaps. *J. Phys. Chem. Lett.* **8**, 1739–1744 (2017).
207. Liu, M., Hu, C., Campbell, J. C., Pan, Z. & Tashima, M. M. Reduce afterpulsing of single photon avalanche diodes using passive quenching with active reset. *IEEE J. Quantum Electron.* **44**, 430–434 (2008).
208. Wang, T., Boer-Duchemin, E., Zhang, Y., Comtet, G. & Dujardin, G. Excitation of propagating surface plasmons with a scanning tunnelling microscope. *Nanotechnology* **22**, 175201 (2011).
209. Wang, K. & Xu, B. Modulation and control of charge transport through single-molecule junctions. *Top. Curr. Chem.* **375**, 17 (2017).
210. Inkpen, M. S. et al. New insights into single-molecule junctions using a robust, unsupervised approach to data collection and analysis. *J. Am. Chem. Soc.* **137**, 9971–9981 (2015).
211. Kos, D. et al. Optical probes of molecules as nano-mechanical switches. *Nat. Commun.* **11**, 5905 (2020).
212. Frederiksen, T. Bimetallic electrodes boost molecular junctions. *Nat. Mater.* **20**, 577–578 (2021).
213. Tserkezis, C. et al. Hybridization of plasmonic antenna and cavity modes: extreme optics of nanoparticle-on-mirror nanogaps. *Phys. Rev. A* **92**, 053811 (2015).
214. Kongsuwan, N. et al. Plasmonic nanocavity modes: from near-field to far-field radiation. *ACS Photonics* **7**, 463–471 (2020).
215. Lalanne, P., Yan, W., Vynck, K., Sauvan, C. & Hugonin, J.-P. Light interaction with photonic and plasmonic resonances. *Laser Photonics Rev.* **12**, 1700113 (2018).
216. Ching, E. S. C. et al. Quasinormal-mode expansion for waves in open systems. *Rev. Mod. Phys.* **70**, 1545–1554 (1998).
217. Leung, P. T., Liu, S. Y. & Young, K. Completeness and time-independent perturbation of the quasinormal modes of an absorptive and leaky cavity. *Phys. Rev. A* **49**, 3982–3989 (1994).
218. Tang, P. et al. Plasmonic particle-on-film nanocavity in tightly focused vector beam: a full-wave theoretical analysis from near-field enhancement to far-field radiation. *Plasmonics* **16**, 215–225 (2021).
219. Horton, M. J. et al. Nanoscopy through a plasmonic nanolens. *Proc. Natl Acad. Sci. USA* **117**, 2275–2281 (2020).
220. Jiang, W., Hu, H., Deng, Q., Zhang, S. & Xu, H. Temperature-dependent dark-field scattering of single plasmonic nanocavity. *Nanophotonics* **9**, 3347–3356 (2020).
221. Chen, X. & Nijhuis, C. A. The unusual dielectric response of large area molecular tunnel junctions probed with impedance spectroscopy. *Adv. Electron. Mater.* **8**, 2100495 (2022).
222. Jiang, L., Sangeeth, C. S. S., Yuan, L., Thompson, D. & Nijhuis, C. A. One-nanometer thin monolayers remove the deleterious effect of substrate defects in molecular tunnel junctions. *Nano Lett.* **15**, 6643–6649 (2015).
223. Cui, X. et al. Molecular tunnel junction-controlled high-order charge transfer plasmon and Fano resonances. *ACS Nano* **12**, 12541–12550 (2018).
224. Zhang, Y. et al. Visualizing coherent intermolecular dipole–dipole coupling in real space. *Nature* **531**, 623–627 (2016).
225. Luk'yanchuk, B. et al. The Fano resonance in plasmonic nanostructures and metamaterials. *Nat. Mater.* **9**, 707–715 (2010).
226. Vardi, Y., Cohen-Hoshen, E., Shalem, G. & Bar-Joseph, I. Fano resonance in an electrically driven plasmonic device. *Nano Lett.* **16**, 748–752 (2016).
227. Sanders, A. et al. Understanding the plasmonics of nanostructured atomic force microscopy tips. *Appl. Phys. Lett.* **109**, 153110 (2016).
228. Gutzler, R., Garg, M., Ast, C. R., Kuhnke, K. & Kern, K. Light–matter interaction at atomic scales. *Nat. Rev. Phys.* **3**, 441–453 (2021).
This work is a comprehensive review of electromagnetic radiation on STM tunnelling junctions.
229. Aizpurua, J., Apell, S. P. & Berndt, R. Role of tip shape in light emission from the scanning tunneling microscope. *Phys. Rev. B* **62**, 2065–2073 (2000).
230. Dong, Z. C. et al. Generation of molecular hot electroluminescence by resonant nanocavity plasmons. *Nat. Photon.* **4**, 50–54 (2010).
231. Taminiau, T. H., Moerland, R. J., Segerink, F. B., Kuipers, L. & van Hulst, N. F. $\lambda/4$ resonance of an optical monopole antenna probed by single molecule fluorescence. *Nano Lett.* **7**, 28–33 (2007).
232. Höppener, C. & Novotny, L. Antenna-based optical imaging of single Ca^{2+} transmembrane proteins in liquids. *Nano Lett.* **8**, 642–646 (2008).
233. Böckmann, H. et al. Near-field manipulation in a scanning tunneling microscope junction with plasmonic Fabry–Pérot tips. *Nano Lett.* **19**, 3597–3602 (2019).
234. Reddy, H. et al. Determining plasmonic hot-carrier energy distributions via single-molecule transport measurements. *Science* **369**, 423–426 (2020).
This work is a detailed study on the conductance contribution of hot electrons by plasmonic excitation.
235. May, M. A. et al. Nano-cavity QED with tunable nano-tip interaction. *Adv. Quantum Technol.* **3**, 1900087 (2020).
236. Jaculbia, R. B. et al. Single-molecule resonance Raman effect in a plasmonic nanocavity. *Nat. Nanotech* **15**, 105–110 (2020).
237. Kumar, N., Weckhuysen, B. M., Wain, A. J. & Pollard, A. J. Nanoscale chemical imaging using tip-enhanced Raman spectroscopy. *Nat. Protoc.* **14**, 1169–1193 (2019).
238. Ojambati, O. S. et al. Efficient generation of two-photon excited phosphorescence from molecules in plasmonic nanocavities. *Nano Lett.* **20**, 4653–4658 (2020).
239. Große, C. et al. Dynamic control of plasmon generation by an individual quantum system. *Nano Lett.* **14**, 5693–5697 (2014).
240. Rai, V. et al. Boosting light emission from single hydrogen phthalocyanine molecules by charging. *Nano Lett.* **20**, 7600–7605 (2020).
241. Chong, M. C. et al. Ordinary and hot electroluminescence from single-molecule devices: controlling the emission color by chemical engineering. *Nano Lett.* **16**, 6480–6484 (2016).
242. Doppagne, B. et al. Electrofluorochromism at the single-molecule level. *Science* **361**, 251–255 (2018).
243. Zhu, S.-E. et al. Self-decoupled porphyrin with a tripodal anchor for molecular-scale electroluminescence. *J. Am. Chem. Soc.* **135**, 15794–15800 (2013).
244. Xu, F., Holmqvist, C. & Belzig, W. Overbias light emission due to higher-order quantum noise in a tunnel junction. *Phys. Rev. Lett.* **113**, 066801 (2014).
245. Schull, G., Néel, N., Johansson, P. & Berndt, R. Electron–plasmon and electron–electron interactions at a single atom contact. *Phys. Rev. Lett.* **102**, 057401 (2009).
246. Kuhnke, K., Große, C., Merino, P. & Kern, K. Atomic-scale imaging and spectroscopy of electroluminescence at molecular interfaces. *Chem. Rev.* **117**, 5174–5222 (2017).
247. Zhang, Y. et al. Sub-nanometre control of the coherent interaction between a single molecule and a plasmonic nanocavity. *Nat. Commun.* **8**, 15225 (2017).
248. Böckmann, H. et al. Near-field spectral response of optically excited scanning tunneling microscope junctions probed by single-molecule action spectroscopy. *J. Phys. Chem. Lett.* **10**, 2068–2074 (2019).
249. Carnegie, C. et al. Room-temperature optical picocavities below 1 nm^3 accessing single-atom geometries. *J. Phys. Chem. Lett.* **9**, 7146–7151 (2018).
250. Benz, F. et al. Single-molecule optomechanics in "picocavities". *Science* **354**, 726–729 (2016).
251. Lindquist, N. C. & Brolo, A. G. Ultra-high-speed dynamics in surface-enhanced Raman scattering. *J. Phys. Chem. C* **125**, 7523–7532 (2021).
252. Lindquist, N. C., de Albuquerque, C. D. L., Sobral-Filho, R. G., Paci, I. & Brolo, A. G. High-speed imaging of surface-enhanced Raman scattering fluctuations from individual nanoparticles. *Nat. Nanotech.* **14**, 981–987 (2019).
253. Bido, A. T., Nordberg, B. G., Engevik, M. A., Lindquist, N. C. & Brolo, A. G. High-speed fluctuations in surface-enhanced Raman scattering intensities from various nanostructures. *Appl. Spectrosc.* **74**, 1398–1406 (2020).
254. Kamp, M. et al. Cascaded nanooptics to probe microsecond atomic-scale phenomena. *Proc. Natl. Acad. Sci. USA* **117**, 14819–14826 (2020).
255. Li, C.-Y. et al. Real-time detection of single-molecule reaction by plasmon-enhanced spectroscopy. *Sci. Adv.* **6**, eaba6012 (2020).
256. Moerner, W. E., Shechtman, Y. & Wang, Q. Single-molecule spectroscopy and imaging over the decades. *Faraday Discuss.* **184**, 9–36 (2015).
257. Huang, D. et al. Photoluminescence of a plasmonic molecule. *ACS Nano* **9**, 7072–7079 (2015).
258. Carnegie, C. et al. Flickering nanometre-scale disorder in a crystal lattice tracked by plasmonic flare light emission. *Nat. Commun.* **11**, 682 (2020).
259. Chen, W. et al. Intrinsic luminescence blinking from plasmonic nanojunctions. *Nat. Commun.* **12**, 2731 (2021).
260. Chikkaraddy, R. et al. Mapping nanoscale hotspots with single-molecule emitters assembled into plasmonic nanocavities using DNA origami. *Nano Lett.* **18**, 405–411 (2018).
261. Lombardi, A. et al. Pulsed molecular optomechanics in plasmonic nanocavities: from nonlinear vibrational instabilities to bond-breaking. *Phys. Rev. X* **8**, 011016 (2018).
262. Ojambati, O. S. et al. Quantum electrodynamics at room temperature coupling a single vibrating molecule with a plasmonic nanocavity. *Nat. Commun.* **10**, 1049 (2019).
263. Choi, H.-K. et al. Metal-catalyzed chemical reaction of single molecules directly probed by vibrational spectroscopy. *J. Am. Chem. Soc.* **138**, 4673–4684 (2016).
264. Li, L. et al. Metal oxide nanoparticle mediated enhanced Raman scattering and its use in direct monitoring of interfacial chemical reactions. *Nano Lett.* **12**, 4242–4246 (2012).
265. Galego, J., Climent, C., Garcia-Vidal, F. J. & Feist, J. Cavity Casimir–Polder forces and their effects in ground-state chemical reactivity. *Phys. Rev. X* **9**, 021057 (2019).
266. Kongsuwan, N. et al. Suppressed quenching and strong-coupling of Purcell-enhanced single-molecule emission in plasmonic nanocavities. *ACS Photonics* **5**, 186–191 (2018).
267. Akselrod, G. M. et al. Probing the mechanisms of large Purcell enhancement in plasmonic nanoantennas. *Nat. Photon.* **8**, 835–840 (2014).
268. Yang, B. et al. Sub-nanometre resolution in single-molecule photoluminescence imaging. *Nat. Photon* **14**, 693–699 (2020).
269. Sáez-Blázquez, R., Feist, J., Fernández-Domínguez, A. I. & García-Vidal, F. J. Enhancing photon correlations through plasmonic strong coupling. *Optica* **4**, 1363–1367 (2017).

270. Sáez-Blázquez, R., Feist, J., García-Vidal, F. J. & Fernández-Domínguez, A. I. Photon statistics in collective strong coupling: nanocavities and microcavities. *Phys. Rev. A.* **98**, 013839 (2018).
271. Fernández-Domínguez, A. I., Bozhevolnyi, S. I. & Mortensen, N. A. Plasmon-enhanced generation of nonclassical light. *ACS Photonics* **5**, 3447–3451 (2018).
272. Maier, S. A. in *Plasmonics: Fundamentals and Applications* (ed. Maier, S. A.) 89–104 (Springer US, 2007).
273. Barnes, W. L., Dereux, A. & Ebbesen, T. W. Surface plasmon subwavelength optics. *Nature* **424**, 824–830 (2003).
274. Sital, S. Surface plasmon modes of dielectric–metal–dielectric waveguides and applications. *IOSR J. Electr. Electron. Eng.* **12**, 08–19 (2017).
275. Valmorra, F. et al. Strong coupling between surface plasmon polariton and laser dye rhodamine 800. *Appl. Phys. Lett.* **99**, 051110 (2011).
276. Cade, N. I., Ritman-Meer, T. & Richards, D. Strong coupling of localized plasmons and molecular excitons in nanostructured silver films. *Phys. Rev. B* **79**, 241404 (2009).
277. Smolyaninov, I. I., Hung, Y.-J. & Davis, C. C. Surface plasmon dielectric waveguides. *Appl. Phys. Lett.* **87**, 241106 (2005).
278. Ditlbacher, H. et al. Coupling dielectric waveguide modes to surface plasmon polaritons. *Opt. Express* **16**, 10455–10464 (2008).
279. Ahmed Ammar, R. & LEMERINI, M. Surface plasmon polariton in metal–insulator–metal configuration. *Int. J. Nanoelectronics Mater.* **10**, 185–194 (2017).
280. Wang, T., Du, W., Tomczak, N., Wang, L. & Nijhuis, C. A. In operando characterization and control over intermittent light emission from molecular tunnel junctions via molecular backbone rigidity. *Adv. Sci.* **6**, 1900390 (2019).
281. Tefashe, U. M., Van Dyck, C., Saxena, S. K., Lacroix, J.-C. & McCreery, R. L. Unipolar injection and bipolar transport in electroluminescent Ru-centered molecular electronic junctions. *J. Phys. Chem. C.* **123**, 29162–29172 (2019).
282. van Nguyen, Q. et al. Molecular signature and activationless transport in cobalt-terpyridine-based molecular junctions. *Adv. Electron. Mater.* **6**, 1901416 (2020).
283. Supur, M., Saxena, S. K. & McCreery, R. L. Ion-assisted resonant injection and charge storage in carbon-based molecular junctions. *J. Am. Chem. Soc.* **142**, 11658–11662 (2020).
284. Hwang, W.-T., Jang, Y., Song, M., Xiang, D. & Lee, T. Large-area molecular monolayer-based electronic junctions with transferred top electrodes. *Jpn. J. Appl. Phys.* **59**, SD0803 (2020).
285. Jeong, H. et al. Redox-induced asymmetric electrical characteristics of ferrocene-alkanethiolate molecular devices on rigid and flexible substrates. *Adv. Funct. Mater.* **24**, 2472–2480 (2014).
286. Koo, J. et al. Unidirectional real-time photoswitching of diarylethene molecular monolayer junctions with multilayer graphene electrodes. *ACS Appl. Mater. Inter.* **11**, 11645–11653 (2019).
287. Nijhuis, C. A., Reus, W. F., Barber, J. R. & Whitesides, G. M. Comparison of SAM-based junctions with Ga_2O_3/EGaIn top electrodes to other large-area tunneling junctions. *J. Phys. Chem. C* **116**, 14139–14150 (2012).
288. Fereiro, J. A., Kondratenko, M., Bergren, A. J. & McCreery, R. L. Internal photoemission in molecular junctions: parameters for interfacial barrier determinations. *J. Am. Chem. Soc.* **137**, 1296–1304 (2015).
289. Du, W. et al. On-chip molecular electronic plasmon sources based on self-assembled monolayer tunnel junctions. *Nat. Photon.* **10**, 274–280 (2016).
290. Han, Y. & Nijhuis, C. A. Functional redox-active molecular tunnel junctions. *Chem. Asian J.* **15**, 3752–3770 (2020).
291. Du, W. et al. Directional excitation of surface plasmon polaritons via molecular through-bond tunneling across double-barrier tunnel junctions. *Nano Lett.* **19**, 4634–4640 (2019).
292. Selzer, Y. Elucidating the contributions of plasmon-induced excitons and hot carriers to the photocurrent of molecular junctions. *J. Phys. Chem. C* **124**, 8680–8688 (2020).
293. Furuya, R., Omagari, S., Tan, Q., Lokstein, H. & Vacha, M. Enhancement of the photocurrent of a single photosystem I complex by the localized plasmon of a gold nanorod. *J. Am. Chem. Soc.* **143**, 13167–13174 (2021).
294. Conklin, D. et al. Exploiting plasmon-induced hot electrons in molecular electronic devices. *ACS Nano* **7**, 4479–4486 (2013).
295. Zhang, J. et al. Enhanced photoresponse of conductive polymer nanowires embedded with Au nanoparticles. *Adv. Mater.* **28**, 2978–2982 (2016).
296. Ai, Y., Nguyen, V. Q., Ghilane, J., Lacaze, P.-C. & Lacroix, J.-C. Plasmon-induced conductance switching of an electroactive conjugated polymer nanojunction. *ACS Appl. Mater. Inter.* **9**, 27817–27824 (2017).
297. de Nijs, B. et al. Plasmonic tunnel junctions for single-molecule redox chemistry. *Nat. Commun.* **8**, 994 (2017).
298. Zheng, J. et al. Electrical and SERS detection of disulfide-mediated dimerization in single-molecule benzene-1,4-dithiol junctions. *Chem. Sci.* **9**, 5033–5038 (2018).
299. Guo, J. et al. Monitoring the dynamic process of formation of plasmonic molecular junctions during single nanoparticle collisions. *Small* **14**, 1704164 (2018).
300. Punj, D. et al. Plasmonic antennas and zero-mode waveguides to enhance single molecule fluorescence detection and fluorescence correlation spectroscopy toward physiological concentrations. *Wiley Interdiscip. Rev. Nanomed. Nanobiotechnol.* **6**, 268–282 (2014).
301. Puchkova, A. et al. DNA origami nanoantennas with over 5000-fold fluorescence enhancement and single-molecule detection at 25 μM. *Nano Lett.* **15**, 8354–8359 (2015).
302. Acuna, G. P. et al. Fluorescence enhancement at docking sites of DNA-directed self-assembled nanoantennas. *Science* **338**, 506–510 (2012).
303. Nusz, G. J. et al. Label-free plasmonic detection of biomolecular binding by a single gold nanorod. *Anal. Chem.* **80**, 984–989 (2008).
304. Li, X., Tang, B., Wu, B., Hsu, C. & Wang, X. Highly sensitive diffraction grating of hydrogels as sensors for carbon dioxide detection. *Ind. Eng. Chem. Res.* **60**, 4639–4649 (2021).
305. Taylor, A. B. & Zijlstra, P. Single-molecule plasmon sensing: current status and future prospects. *ACS Sens.* **2**, 1103–1122 (2017).
306. Yang, Y. et al. Roadmap for single-molecule surface-enhanced Raman spectroscopy. *Adv. Photonics* **2**, 014002 (2020).
307. Kim, J.-M. et al. Synthesis, assembly, optical properties, and sensing applications of plasmonic gap nanostructures. *Adv. Mater.* **33**, 2006966 (2021).
308. Bouloumis, T. D. & Nic Chormaic, S. From far-field to near-field micro- and nanoparticle optical trapping. *Appl. Sci.* **10**, 1375 (2020).
309. Zhang, Y. et al. Plasmonic tweezers: for nanoscale optical trapping and beyond. *Light Sci. Appl.* **10**, 59 (2021).
310. Huang, J.-A. et al. SERS discrimination of single DNA bases in single oligonucleotides by electro-plasmonic trapping. *Nat. Commun.* **10**, 5321 (2019).
311. Kitahama, Y., Funaoka, M. & Ozaki, Y. Plasmon-enhanced optical tweezers for single molecules on and near a colloidal silver nanoaggregate. *J. Phys. Chem. C.* **123**, 18001–18006 (2019).
312. Belkin, M., Chao, S.-H., Jonsson, M. P., Dekker, C. & Aksimentiev, A. Plasmonic nanopores for trapping, controlling displacement, and sequencing of DNA. *ACS Nano* **9**, 10598–10611 (2015).
313. Zhan, C. et al. Single-molecule plasmonic optical trapping. *Matter* **3**, 1350–1360 (2020).
314. Aragonès, A. C. & Domke, K. F. Nearfield trapping increases lifetime of single-molecule junction by one order of magnitude. *Cell Rep. Phys. Sci.* **2**, 100389 (2021).
315. Qian, H. et al. Efficient light generation from enhanced inelastic electron tunnelling. *Nat. Photon.* **12**, 485–488 (2018).
316. Kern, J. et al. Electrically driven optical antennas. *Nat. Photon.* **9**, 582–586 (2015).
317. Huang, J. et al. Plasmon-induced trap state emission from single quantum dots. *Phys. Rev. Lett.* **126**, 047402 (2021).
318. Zhang, W., Caldarola, M., Lu, X. & Orrit, M. Plasmonic enhancement of two-photon-excited luminescence of single quantum dots by individual gold nanorods. *ACS Photonics* **5**, 2960–2968 (2018).
319. Shen, Q., Hoang, T. B., Yang, G., Wheeler, V. D. & Mikkelsen, M. H. Probing the origin of highly-efficient third-harmonic generation in plasmonic nanogaps. *Opt. Express* **26**, 20718–20725 (2018).
320. Kauranen, M. & Zayats, A. V. Nonlinear plasmonics. *Nat. Photon.* **6**, 737–748 (2012).
321. Zhu, Y., Cui, L. & Natelson, D. Hot-carrier enhanced light emission: the origin of above-threshold photons from electrically driven plasmonic tunnel junctions. *J. Appl. Phys.* **128**, 233105 (2020).
322. Buret, M. et al. Spontaneous hot-electron light emission from electron-fed optical antennas. *Nano Lett.* **15**, 5811–5818 (2015).
323. Malinowski, T., Klein, H. R., Iazykov, M. & Dumas, P. Infrared light emission from nano hot electron gas created in atomic point contacts. *EPL* **114**, 57002 (2016).
324. Wu, X., Wang, R., Zhang, Y., Song, B. & Yam, C. Controllable single-molecule light emission by selective charge injection in scanning tunneling microscopy. *J. Phys. Chem. C* **123**, 15761–15768 (2019).
325. Li, Y. et al. Gate controlling of quantum interference and direct observation of anti-resonances in single molecule charge transport. *Nat. Mater.* **18**, 357–363 (2019).
326. Giguère, A., Ernzerhof, M. & Mayou, D. Surface plasmon polariton-controlled molecular switch. *J. Phys. Chem. C* **122**, 20083–20089 (2018).
327. Chen, S., Liu, J., Lu, H. & Zhu, Y. All-optical strong coupling switches based on a coupled meta-atom and MIM nanocavity configuration. *Plasmonics* **8**, 1439–1444 (2013).
328. Wu, Y. et al. Double-wavelength nanolaser based on strong coupling of localized and propagating surface plasmon. *J. Phys. D Appl. Phys.* **53**, 135108 (2020).
329. Urban, A. S. et al. Optical trapping and manipulation of plasmonic nanoparticles: fundamentals, applications, and perspectives. *Nanoscale* **6**, 4458–4474 (2014).
330. Mejía, L., Kleinekathoefer, U. & Franco, I. Coherent and incoherent contributions to molecular electron transport. *J. Chem. Phys.* **156**, 094302 (2022).
331. Saxena, S. K., Smith, S. R., Supur, M. & McCreery, R. L. Light-stimulated charge transport in bilayer molecular junctions for photodetection. *Adv. Optical Mater.* **7**, 1901053 (2019).
332. Ament, I., Prasad, J., Henkel, A., Schmachtel, S. & Soennichsen, C. Single unlabeled protein detection on individual plasmonic nanoparticles. *Nano Lett.* **12**, 1092–1095 (2012).

Acknowledgements
The authors thank J. J. Baumberg, J. Aizpurua, P. Leiderer, J. Boneberg, J. C. Cuevas, F. Pauly, H. Liu and T. Huhn for fruitful discussions. They acknowledge financial support from the National Key R&D Program of China (2021YFA1200103), National Natural Science Foundation of China (91950116, 61571242, 62071318), Natural Science Foundation of Tianjin (19JCZDJC31000, 19JCYBJC16500) and National Research Foundation of Korea (NRF) grants (No. 2021R1A2C3004783 and NRF-2021R1C1C1010266). The authors acknowledge the National Research Foundation (NRF) for supporting this research under the Prime Minister's Office, Singapore, under its Medium-Sized Centre Programme and the Competitive Research Programme (NRF-CRP17-2017-08), as well as the Deutsche Forschungsgemeinschaft (DFG) through SFB 767 (project number 32152442).

Author contributions
T.L., D.X. and C.A.N conceived the outline. M.W., T.W., O.S.O., T.J.D., E.S. and K.K. wrote the manuscript. All authors contributed to discussions, editing and corrections. E.S., D.X. and C.A.N revised the manuscript before the final submission.

Competing interests
The authors declare no competing interests.

Peer review infomation
Nature Reviews Chemistry thanks J. Baumberg, A. Dhawan, Z.-C. Dong, and J.-C. Lacroix for their contribution to the peer review of this work.

Publisher's note
Springer Nature remains neutral with regard to jurisdictional claims in published maps and institutional affiliations.